6-2014

The Optimization of Porosity and Pore Patterning for Patient-Specific Ti-6 Al-4V Femur Implants

Stephen Paolicelli
Union College - Schenectady, NY

The Optimization of Porosity and Pore Patterning for Patient-Specific Ti-6Al-4V Femur Implants

By

S. Alex Paolicelli

****

Submitted in partial fulfillment
of the requirements for
Honors in the Department of Mechanical Engineering

UNION COLLEGE
June 2014

ABSTRACT

PAOLICELLI, S. ALEX The Optimization of Porosity and Pore Patterning for Patient-Specific Ti-6Al-4V Femur Implants
Department of Mechanical Engineering, June 2014

ADVISOR: Professor Glenn P. Sanders, Department of Mechanical Engineering

Metastatic bone cancer often arises in the long bones of the body. Taking a patient specific approach by utilizing a customized implant is a superior method of treatment compared to today's solutions, which often includes amputation. A titanium-alloy femur implant has been optimized by varying pore size, pore pattern, and porosity in order to maximize osseointegration. By maximizing osseointegration, the implant will remain firmly in place for a longer period of time because bone will grow throughout the implant, securing it. In addition, it is important for the bone to behave mechanically like bone. This requires the global elastic modulus of the implant to decrease from 115 GPa to a value between 10-20 GPa, the elastic modulus of the femur. The final design has an effective elastic modulus of 17.6 GPa and has a global porosity of 54%. This design has been analyzed for typical loads a patient may experience such as walking, running, and jumping using finite element analysis. Furthermore, this design has been manufacturing using a 3D printing process. Mechanical loading tests have been performed to compare the results with the FEA results and 3D printing has been evaluated as a method for custom implant manufacturing.

TABLE OF CONTENT

EXECUTIVE SUMMARY

Metastatic bone cancer often arises in the long bones of the body. Unfortunately, amputation of the infected limb is the standard medical treatment for this form of cancer. However, by taking a patient specific approach, the entire leg may be saved by utilizing a customized metal implant. I have optimized a titanium-alloy femur implant by varying pore size, pore pattern, and porosity of the implant to maximize osseointegration. By maximizing osseointegration, the implant will remain firmly in place for a longer period of time because bone will grow throughout the implant, increasing the life of the implant. To promote osseointegration, it is necessary for the implant to mechanically behave similarly to the bone around it. While titanium is a favorable material for medical implants because of its inertness, its elastic modulus is 118 GPa, nearly 8 times larger than that of bone. By increasing porosity of the implant, the effective elastic modulus will decrease, making the implant behave more like bone and thus increasing osseointegration. Through computer-aided design physiologic forces were simulated to test various pore patterns using finite element analyses. The effects of circular, square, and triangular shapes on the effective elastic modulus were assessed. It was concluded that when testing different pore shapes of the same area there is a minimal effect on the modulus; however, stress concentrations around the edges of the square and triangle pores were nearly 60% higher than the stress concentrations around the circular pores. Additionally, the pore pattern has a significant impact on the modulus of the implant. Axially applied pores are much more effective at lowering the elastic modulus then transversely applied pores; although, a combination of both patterns is most effective. Through these conclusions, an optimized femur implant was designed with circular pores

applied both axially and transversely. This design was tested for typical loads a patient may experience such as walking, running, and jumping. The final CAD design has an effective elastic modulus of 17.6 GPa, within the elastic modulus range of 10-20 GPa for bone, and has a global porosity of 54%. Furthermore, this design has been manufacturing using a 3D printing process. Compression tests were performed on the implant and an extensometer was used to measure strain. Compressive loads of 600N and 1200N were applied to the implant and measurements were recorded. The elastic modulus of the implant was measured to be 700 MPa. This value, smaller than the value that FEA predicted, is the result of several different factors. The material printed was 85% dense, compared to the specified density of 99% and had defects including pore size, pore shape, and a crack that was on the lateral side of the implant. This, paired with the limitations of finite element analysis on porous parts, explains the discrepancy in the measured values of elastic moduli for the titanium femur implant.

BACKGROUND:

The Femur

Bones are rigid organs made up of osseous tissue, a relatively hard and lightweight composite material[1]. They serve to provide structure and support for the human body as well as act as a nutrient reserve by hosting bone marrow in the interior of the bone. Bone is composed of two distinct structural materials: cortical bone and cancellous bone. Cortical bone is responsible for supporting the body and protecting organs. It is much more dense and stronger than cancellous bone. Cancellous bone,

found at the ends of long bones, has a higher surface area than cortical bone and contains red bone marrow.

The largest bone in the human body is the femur bone. The femur bone is the most proximal bone in the leg, meaning that it is closest to the core of the body. The head of the femur, in combination with the acetabulum in the pelvic bone, form the hip joint, while the distal part of the femur, in combination with the tibia and patella, form the knee joint. The femur is divided into three sections: the epiphysis, the metaphysis, and the diaphysis. The epiphysis is at each end of long bones such as the femur and humerus. Going towards the middle of the bone, the metaphysis is next. The metaphysis is the transition zone between the epiphysis and diaphysis and contains a large amount of cancellous bone. The middle section of the bone, the diaphysis, is made up of cortical bone.

Inside the femur is a medullary cavity. The medullary cavity, or medullary canal, is also present in long bones of the body. It serves the purpose of storing bone marrow and has walls composed of stiff cortical bone. The cavity is lined with a thin, vascular membrane[2]. The medullary cavity causes the bone to be hollow. Below is a figure of the structure of the femur.

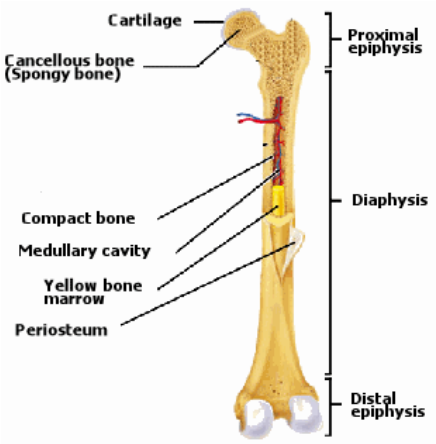

Figure 1: Shows the basic structure of the femur.

Bone behaves well under compression, with a compressive strength of 170 MPa, but is less effective in tension, with a tensile strength of 110 MPa[3]. This allows bones to handle repetitive loading effectively. In certain categories, such as compressive strength, the femur bone is the strongest bone in the human body. These repetitive moments are exerted on the bone every day from standing, walking, or climbing stairs and cause tension in the lateral side of the femur and compression in the medial side of the femur. In addition to the compressive and tensile strength, the elastic modulus of cortical bone ranges from 10-20 GPa[4]. However, despite being structurally sound, there are diseases and illnesses that can start or spread to the femur that can weaken or destroy the bone.

Bone Cancer and Current Treatments

Metastatic bone cancer, cancer that starts somewhere other than bone and then spreads to the bone, is a common form of cancer that generally occurs in young adults but can affect people of all ages. Other bone cancers, such as osteosarcoma, chondrosarcoma, and Ewing's sarcoma, in which the cancer originates in the bone, is much more rare than metastatic bone cancer. Metastatic bone cancer, along with primary

bone cancer, often grows in the long bones of the body, especially in the femur, and cause severe pain, described by a dull, and constant ache[5]. There are over 1.2 million new cases of metastatic bone cancer and about 2,300 new cases of primary bone cancer each year[6].

Figure 2: Shows a cancerous tumor in a femur.

Metastatic and primary bone cancers, as well as all other types of cancer, result from unregulated cell growth. Cells divide and grow irrepressibly, forming a lump called a tumor and may spread to other parts of the body. Commonly, when cancer develops in the femur, there are options for treatment such as amputation or the implementation of an endoprosthesis. Clearly, amputation is not an ideal form of treatment. Fully or partially removing the leg of the patient will drastically decrease mobility and have a lasting effect on the patient's comfort and quality of life. While in some cases, this may be the only possible treatment to eradicate the cancer; it is not the preferred method. Another option is the implantation of an endoprosthesis. An endoprosthesis is an artificial device used to

replace a body part and is placed inside the body during surgery. An endoprosthesis, depending on where the cancer is located in the femur, may result in removing part of the knee to securely place the implant in the patient. If this is necessary, this will lead to discomfort to the patient and decreases their mobility. Part of this discomfort arises from loosening or failure of the implant. This loosening may arise from the forces the endoprosthesis faces on a regular basis, as well as wear particles that result from continuous loading. Stress shielding, which is a reduction in the stress of the bone due to a more rigid metallic implant, can also lead to bone resorption. Consequently, this loosening or failure is a major drawback for this treatment. Whenever the knee joint is altered, severe physical therapy is necessary and it becomes difficult to fully regain mobility. Below is a picture of an endoprosthesis placed in the femur. Note that the femoral portion of the knee joint and portion of the tibia has been removed from the patient in order to fit the implant.

Figure 3: Shows the implementation of an endoprosthesis.

While this method is a better alternative to amputation, if the endoprosthesis fails, amputation then becomes necessary. Both treatments have their major flaws and setbacks. In addition to these, there are some current methods that are aimed at minimizing amputation by simply removing only the cancerous portion of the bone. Doctors use allografts to replace the removed bones. Bone grafting is a surgical procedure that replaces sections of bones that have been removed. An allograft is a graft received by the patient from another person, generally a cadaveric donor. Grafting poses a significant health risk to the patient also because the graft may fail, not heal properly, or the body may treat the graph as a foreign substance and reject it. While using a metal implant poses similar risks, it is less likely to fail mechanically, compared to the weaker allograft.

Unfortunately, the methods for treating this void have limitations. By analyzing the cancer and the adjacent bone, a porous metal implant can be customized and utilized as treatment. The cancerous bone will be removed from the femur and the implant positioned in its place during surgery. The implant is porous so that native bone can become incorporated into the implant and keep the implant firmly in place for the lifetime of the patient. However, if bone does not grow around and through the implant, it can lead to failure of the implant or loosening, causing discomfort to the patient. Additional surgery, and possible amputation, then becomes necessary. Stiffness and porosity has a direct result on how efficiently the implant becomes incorporated with the surrounding bone[7]. Unfortunately, the optimal porosity is not well understood.

Proposed Solution

CT data of an anonymous patient was received from Dr. Matt DiCaprio of Albany Medical Center. This patient had a mid-diaphysis lesion in her left femur. For my senior project, I optimized a femur implant for this patient to promote a higher rate of bone growth. By varying the porosity of the implant, pore size, pore shape, and pore patterning, I hypothesize that it will increase the likelihood of osseointegration in the implant, which theoretically would result in a longer lifetime of the implant and better quality of life for the patient. The implant will be made of a metal alloy rather than allografts or plastics, which is beneficial as metal alloys having a much higher strength. More specifically a titanium alloy is used as the biomaterial for the implant because of its high strength, excellent corrosion resistance, and lightweight.

Ti-6Al-4V (a chemical composition of 6% aluminum, 4% vanadium, 0.25%, iron, 0.2% oxygen, and the remainder titanium) is a titanium alloy that is often used in medical implants. It has an elastic modulus of 118 GPa; while bone typically has an elastic modulus of 10-20 GPa[8]. Elastic modulus is a material property, which describes the material's stiffness normalized to the geometry of the structure. Adding pores to the global structure of the implant will not alter the elastic modulus of the implant; however, it will alter the stiffness of the implant, also called the effective elastic modulus. In this study, pores were altered to control the effective elastic modulus. Ideally, the implant would have a very similar elastic modulus to bone. By having a similar elastic modulus, both the bone and implant would react similarly under loading and bone would grow to account for stress. According to Wolff's law, bone is deposited and reinforced at areas of increased stress[9]. To increase the osseointegration of the implant, it is important to

choose a material with an elastic modulus of under 50 GPa. Conveniently, these implants need to have pores to allow bone to grow in and throughout the implant. By creating pores in the titanium implant, the effective elastic modulus of the implant decreases. By adjusting the porosity, the final implant can approach an elastic modulus similar to the bone it is connecting. Varying several factors of the implant model, such as pore size, pore shape, and pore patterning, will lower the effective elastic modulus and cause the implant to behave mechanically similar to the bone around it. While modifying and optimizing the implant to have an elastic modulus between 10-20 GPa, it is important that the implant still maintain the durability and strength that is required for typical loading that the patient may encounter.

METHODS:

Effective Elastic Modulus

When calculating the modulus of the implant, it is important to understand what role the elastic modulus has on the mechanical behavior of the system. Elastic modulus is a material property relating the strain of a system when a stress is applied to it. Because it is a material property, the elastic modulus of a system made using the same material will never vary, despite manipulations to the geometry and size of the system. This definitive value of elastic modulus is not used when comparing the elastic modulus of the implant to bone. Instead, the effective elastic modulus is used. The effective elastic modulus is the elastic modulus of the entire system, which will vary based on changes to its geometry. For these purposes, the effective elastic modulus will describe the implant much more accurately then using the material's elastic modulus.

Calculation of the Modulus

To calculate the effective elastic modulus of a system, many factors must be taken into consideration. Both the stress and the strain of the implant are dependent on several geometric properties. To calculate the stress applied to the implant, Equation 1 was used:

$$\sigma = \frac{F_A}{A} \quad (1)$$

Where σ is the stress of the implant, F_A is the applied force, and A is the total cross-sectional area that the force is applied to. This applied force on the cross sectional area can be seen more clearly in Figure 4 below:

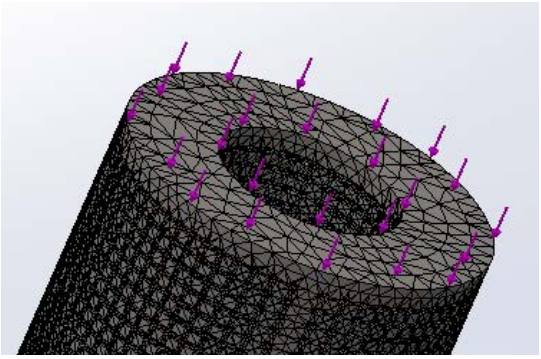

Figure 4: Shows the applied force over the cross-sectional area of a design.

The force of a 160-lb person standing is equivalent to a force of approximately 600N. It is likely that the implant will undergo applied forces ranging from 300N (when the patient is leaning against a wall) to 1500N (when the patient is running or going upstairs) based on an estimated mass of a patient[10].

In order to calculate the strain that results from the applied force, the deformation of the implant must be measured. The formula for deformation is below:

$$\delta = \frac{PL}{AE} \tag{2}$$

Where δ is the deformation of the implant, P is the applied axial force, L is the total length of the implant, A is the area where the force is applied and E is the material's elastic modulus. Using SolidWorks, this deformation, or displacement, can be measured when forces are applied during simulations. Having the change in length of the implant, strain can be calculated.

$$\varepsilon = \frac{\delta}{L} \tag{3}$$

Where ε is strain. Strain is a normalized measure of deformation that represents the displacement in reference to the total length of the object. With the stress calculated and the strain calculated based on the measurement of deformation, Hooke's Law was used to calculate the effective elastic modulus of the system:

$$E = \frac{\sigma}{\varepsilon} \tag{4}$$

Where E is the effective elastic modulus. To get a more accurate value, several different forces were applied to the implant and with each separate force a different displacement was measured. The max displacement was measured in SolidWorks and was converted into a strain based on Equation 3. Then, these values of stress, calculated from the applied force and the area, and the measured values of strain, were plotted. The slope of the plot represents the elastic modulus and denotes the average elastic modulus over the range of forces applied to the implant.

Alternative Calculation of the Modulus

For comparison purposes, an alternative method for estimating the global elastic modulus was examined. Using specific material characteristics, including geometric characteristics of the pores, a global elastic modulus was calculated[11]. Initially, a geometric factor for the pores must be calculated using Equation 5 below.

$$\rho = \frac{4\pi A}{P} \tag{5}$$

Where ρ is the geometric factor, A is the area of a single pore, and P is the perimeter of a single pore. Substituting the formulas for the area of a circle and the circumference of a circle, as the pores used in the design were circular, Equation 5 is simplified to Equation 6.

$$\rho = 2\pi r \tag{6}$$

Having a geometric factor for the pores used in the femur implant, the global elastic modulus for the titanium alloy implant was calculated using Equation 7.

$$E = E_M \left[\frac{(1-\nu)^2}{1+\left(\frac{1}{\rho}-1\right)\nu} \right] \tag{7}$$

Where E is the elastic modulus of the porous implant, E_M is the elastic modulus of the material, and v is the volume fraction of the porosity. The values of the pore geometric factor and volume fraction of porosity varied between the SolidWorks model and the manufactured implant.

Modeling the Implant

To begin the initial tests on the implant, the implant was modeled as a cylinder with an outside diameter of 4.5 cm. The outside diameter was chosen at 4.5 cm based on an average outside diameter of typical femurs in humans. It was assumed that the section of the femur that would be cancerous would be a section in the middle of the femur. Due to the typical anatomy of the shape of the femur, the middle of the femur was modeled as a cylinder.

In general, the actual shape of the femur closely resembles a cylinder; therefore, this model was appropriate for initial simulations and calculations. In addition to this, the medullary cavity was modeled in the implant. This serves two purposes: it decreases elastic modulus of the implant by increasing the surface area of the implant and thus increasing porosity and also mimics the geometry of the femur. Mimicking this shape in the design of the implant further allows the implant to behave similarly to the femur. The diameter of the cavity was set to 2.25 cm, also based on average values[12]. The height of the implant was set to 5.0 cm, a value that was determined based on the cost to manufacture the final design using 3D printers; however, this specific patient's tumor was 15 cm. Tumors can often result in a resection in the range of 12-20 cm. This height was not largely influenced based on the geometry of the femur.

As initial tests were conducted and the application of pores was altered, the model of the implant changed. Details of the simulations performed and the evolution of the pore patterning is discussed thoroughly later in this report. It was desired that caps were placed on the top and bottom of the implant for practical medical applications. Doctors may place bone grafts inside the medullary cavity of the implant to promote

bony ingrowth and osseointegration. Having these removable caps on the top and bottom make this process easier for medical professionals. The addition of these caps increased the overall height of the implant from 5.0 cm to 5.6 cm. Instead of having a medullary cavity through the entire implant, the cavity's height was changed to 5.3 cm, leaving a 1.5 mm cap on the top of the implant and a 1.5 mm cap on the bottom of the implant. This can be view in Figure 5 below.

Figure 5: Shows a cross section view of the femur implant, highlighting the 1.5 mm caps.

In addition to the caps, as modeling became more complex, the cylinder implant was replaced with a cross-section of an actual femur. A patient's femur was imported into SolidWorks and a 5.6 cm section was removed and used as the new model of the implant. Just as done with the previous model, the medullary cavity and two caps were incorporated in the design. This change in modeling occurred only after a coherent understanding on how the porosity influences the elastic modulus of the implant was obtained. The outer diameter and the medullary cavity diameter changed. This is because the dimensions of a specific patient's femur were used. The original model was based off of assumed dimensions while this model was based of dimensions of an actual femur.

The new outside diameter changed from 4.5 cm to 3.0 cm. The ratio of outer diameter to medullary cavity diameter was slightly altered as well from the cylinder model to the femur model. Thus the medullary cavity was 1.60 cm. This final model of the titanium femur implant, representing an actual cross section of a femur, provided an accurate model for finite element analysis in SolidWorks.

Modeling Forces on the Implant

When simulating the forces that the implant may experience under regular use, it is important to apply the forces to the implant in the same manner that they would be applied to in real life. When standing upright, there is an applied force acting downward through the femur as well as a moment acting on the femur. The application of this force is simulated two ways: the force is evenly distributed over the entire top surface of the femur or the force is evenly distributed across the top section of the implant that is in direct contact with the femur. For the second case, the force is not distributed in the middle section of the implant because of the empty space from the medullary cavity. For completeness, both force applications were examined. Forces of 300N, 600N, 900N, 1200N, and 1500N were simulated in SolidWorks to provide a more precise measurement of the elastic modulus of the system. The choice of these forces is two-fold. This range represents expected forces that the implant may experience when the patient is walking, jogging, going up and down stairs and other everyday movement[13]. In addition to this, the standard increments provide an even representation of how the modulus is affected across a large range of different applied forces.

For purposes of these simulations, the bottom of the implant was fixed using a roller/slider fixture. When the implant is compressed in the vertical axis, the implant will

expand in the other two directions that are perpendicular to the direction of compression. This occurrence is known as Poisson's Effect[14]. By implementing a roller/slider fixture, the implant will be able to expand in these two other directions, resulting in a more accurate simulation. Using only a fixed geometry would prevent the implant from expanding in the directions perpendicular to the axis of the implant and cause inaccurate displacements and thus inaccurate measurements of the effective elastic modulus.

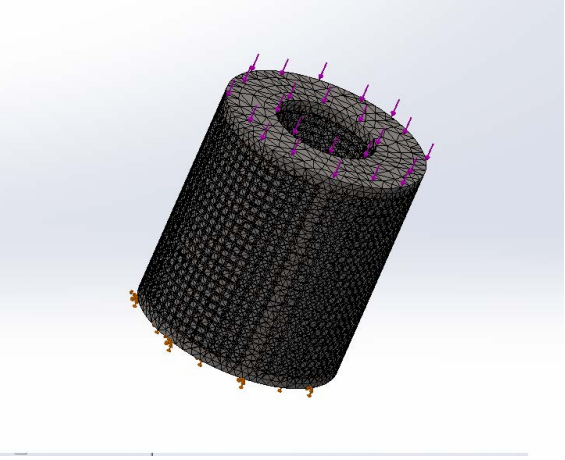

Figure 6: Shows the meshed cylinder model with applied forces and a fixed bottom.

Because the force does not act through the axis of symmetry, a moment is also present. This moment acts on the femur as well as the implant.

Modeling Moment Forces on the Implant

In addition to the vertically applied force, the implant may experience moments due to the geometry of the femur. Because the femur is not a perfect cylinder and because the femur does not have a uniform shape throughout, forces applied at the femoral head will not line up with the center of the axis of the femur. This is illustrated in Figure 7 below:

Figure 7: Shows how a force on the femur will result in a moment based on the direction of the applied force.

If this happens, a moment is experienced. The section cut of the femur for the implant was placed 13.0 cm from where the force acts on the fovea capitis. This force acts 3.0 cm away from the axis of symmetry and acts at an angle of 75.6° to the horizontal[15]. This can be seen in Figure 8 below which shows the location of the implant within the femur.

Figure 8: Shows the location of the implant in the femur.

Using a force of 1588N, 1538N in the axial direction and 395N in the transverse direction, a SolidWorks simulation was performed[16]. Figure 9 below shows the remote load on the femur implant.

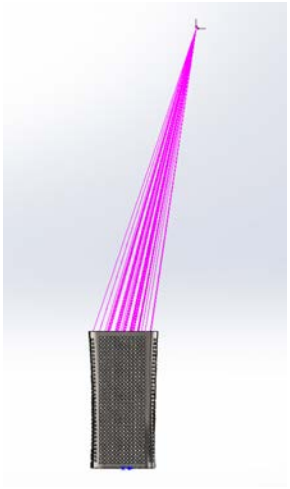

Figure 9: Shows the location of the remote load and the area on the implant it acts.

With this moment applied to the implant, the implant will undergo both tension and compression. Consequently, the internal forces in the implant will vary from location to location. Due to Wolff's law, different portions of the implant, specifically areas close to the neutral axis, will not promote bone growth effectively[17]. Knowing this, varying pore sizes with respect to loading, may be a more apposite method of pore application for a given implant. One such potential solution to this is the incorporation of gradient pores. These pores would increase in size based on the loading of the implant.

The Application of Pores

Essentially, decreasing the effective elastic modulus of the implant from 118 GPa to a value between 10-20 GPa is largely dependent on the application of pores throughout the implant. Increasing porosity of the implant will effectively lower the modulus of the implant. Varying porosity is dependent on the pore shapes and pore patterning in the design of the femur implant. Subsequently, the application of pores is one of the most

important design criteria. Various shapes and patterns were applied to the implant. Squares, circles, and triangles, of equivalent area, were applied axially as well as transversally on multiple planes. The pores were implemented as cuts through the implant using SolidWorks. These cuts went trough the entire implant in the direction in which the pores were applied. It should also be noted that given a specific design, all pores in that design were of the same shape and same area. Varying pore size and pore shape for a particular design was not analyzed. The applications of pores were applied in set patterns as dictated by SolidWorks features. Both linear and circular patterns were explored and compared.

Implant Fabrication

The implant was manufactured using a direct metal laser sintering 3D printer. This specific printer that was used had a layer thickness of 60 μm and had a surface roughness of 125-215 RA. Additionally, the printing orientation can be seen below in Figure 10.

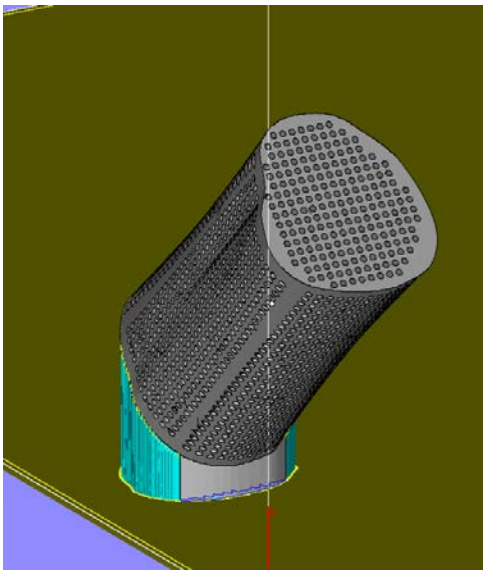

Figure 10: Shows the implant orientation during the printing process.

The implant was printed in less than 24 hours using a high-powered optic laser. There was minor post processing done to the implant after the implant was printed.

Pores Characterization

In order to better understand the direct metal laser sintering 3D printed femur implant, a comparison was done between the pores of the implant and the pores of the computer aided designed implant. The pores of the implant were examined under both a scanning electron microscope and a dissecting microscope. Under the SEM, a sample size of approximately 30 pores on the transverse planes were examined at magnification of 50X – 200X. Due to geometric constraints, only the transversely applied pores were looked at under the SEM.

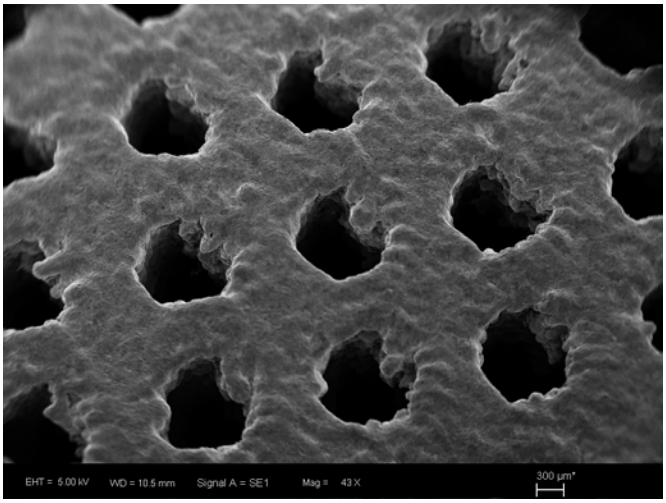

Figure 11: Shows transversely applied pores under a scanning electron microscope.

Under the dissecting microscope, all planes were examined. Because the magnification was 20X – 30X, lower than that of the scanning electron microscope, many more pores were examined. A sample size of approximately 150 pores were examined, 45 of which were specifically measured for dimensions.

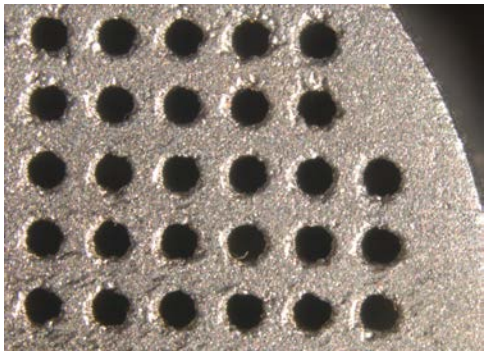

Figure 12: Shows the pores applied axially under a dissecting microscope.

Utilizing ImageJ, a computer software program, 45 pore areas were measured across all three planes. As seen in Figure 12, compared to Figure 11, the pores were inconsistent between planes. The pores applied transversely were smaller in area and less circular compared to the pores applied axially. Using analysis of variance, the pores were analyzed. The characterization of these pores, as well as the implant as a whole, is discussed in the Results section of the report.

Compression Tests

For comparative purposes and to verify the finite element analysis, axial compression tests were performed on the manufactured femur implant. Using an Instru-Met Corporation load frame, compressive loads were applied to the implant at a rate of 0.01 inches/min. The implant was placed within a 9 inch x 9 inch cage to convert the applied tension into applied compression. In addition, the implant was placed on a spherical platen. This platen allows the implant to deform uniformly based on the perpendicular compressive forces. The setup can be seen in Figure 13.

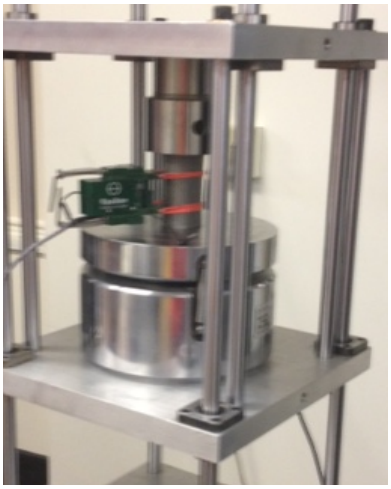

Figure 13: Shows the experimental setup for compression tests.

A Window's based computer program, Test Works, was used to record the compression data. To measure strain during the tests, an extensometer was used. An E80664 extensometer with a gauge length of 1 inch was attached to the lateral side of the femur implant. Once all measurements were zeroed, displacement-controlled compression was conducted until loads of 600N and 1200N were applied to the implant successively. This was done four times to provide eight different sets of data.

RESULTS:

Pore Shapes

Initially, the pore shapes were analyzed in SolidWorks. Squares, triangles, and circles were used as pores. To simplify the comparison between the three different shapes, the pores were applied only axially and not transversely. This allowed for an easy comparison between the elastic moduli of each design. The area of each pore was kept constant as well. This area was 7.85×10^{-7} m. This resulted in a circular pore diameter of 1.0 mm, square pore sides of 0.886 mm, and a base and height of the triangle

pores of 1.3 mm. The applications of the pores were the same as well, being applied in a circular pattern across the top plane of the femur implant. These pore shapes can be seen in Figure 14 below.

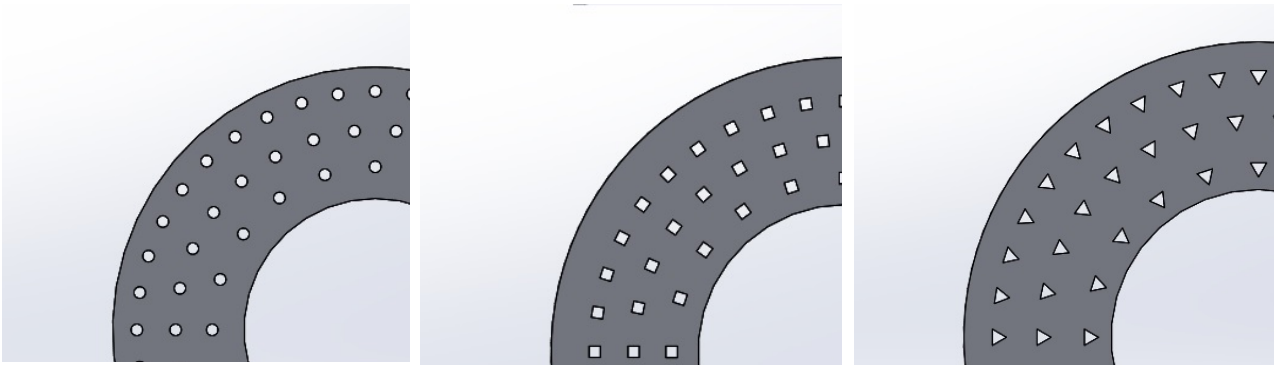

Figure 14: Shows the different shapes considered for pore application: circles, squares, and triangles.

Because all external factors, such as pore application, number of pores, and pore areas, were kept constant, the effect of pore shapes on altering the effective elastic modulus was isolated. It was observed that the shape of the pores did not have a large influence of affecting the elastic modulus. This result was expected based on the deformation equation, Equation 2. Because the force, area, length, and elastic modulus were kept constant, the deformation should remain the same. With the same deformation under similar applied forces, the effective elastic modulus should not vary. However, the pore shape did have an effect on the stress concentrations of the implant. These results, as well as the modulus results are summarized in Table 1 below.

Table 1: Shows the relationship between the elastic modulus and max stress with respect to pore shape.

Shape	Elastic Modulus (GPa)	Stress Concentration (kPa)
Circles	98.0	333
Squares	98.2	532
Triangles	98.5	528

It should be noted that the stress concentrations are nearly 60% higher in the square and triangle pores than the circular pores. The squares and triangles have higher stress concentrations due to their inherent geometry. Because these shapes have corners, they are not able to distribute stress as well as a circle can, a shape with no corners. As a consequence to the corners of squares and triangles, the stress values around the pores will be significantly higher than that of circular pores. Having high stress concentrations could result in an overall weaker design compared to a similar design with smaller stress concentrations. Thus, it has been concluded that circular pores are the most effective shape for lowering the effective elastic modulus while keeping the stress concentrations to a minimum.

Pore Patterning

After a pore shape was determined, the application of the pores were considered. The pattern of the pores could be applied in any 3D direction, using circular patterns or linear patterns. First, the direction of the pores was analyzed. Pores were applied axially,

transversally, and a combination of axial pores and transverse pores. Just as was done in manipulating the pore shapes, all other factors were kept constant for the implant. The exception to this was the number of pores applied. Because the area of which the pores were applied was different, the number of pores in each design was different. Despite this lone inconsistency, the simulations allowed for an accurate comparison between the different patterns. In Figure 15 below, are models where pores were applied axially and pores were applied transversally.

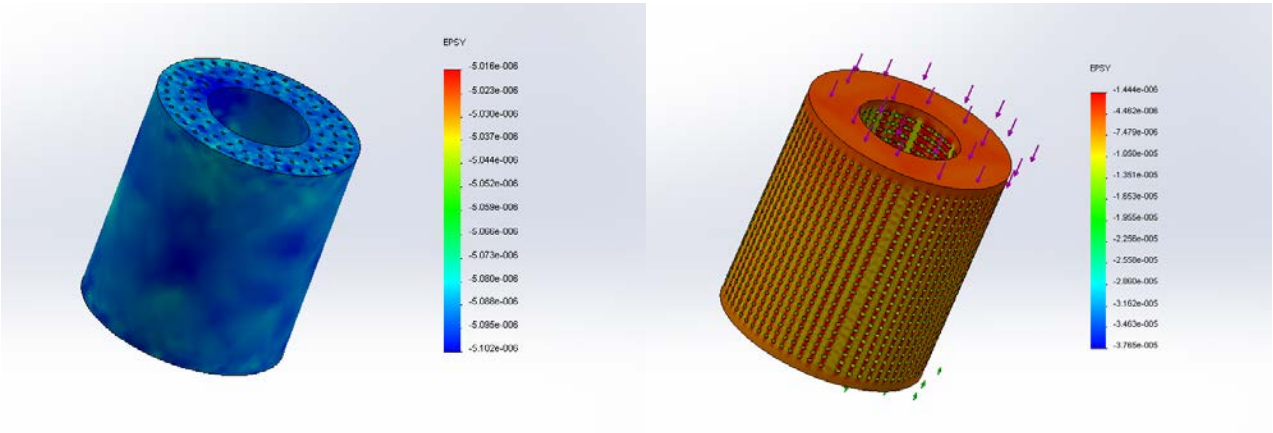

Figure 15: Shows two different pore patterns: axial and transvers.

It was observed through simulation that axially applied pores were much more effective at lowering the elastic modulus of the implant compared to the transversally applied pores. The resulting modulus of the axial design was 77.8 GPa, 29.9 GPa less than the resulting modulus of the transversally applied pores, which was 107.7 GPa. However, using a combination of both pore applications yielded an even lower effective elastic modulus of 59.5 GPa. Using a hybrid of patterns was determined as the most effective way to lower the modulus of the femur implant.

Knowing that both patterns were to be used to lower the effective elastic modulus, the axial pattern of the pores was further explored. The pores on the top surface of the

implant could be applied in a linear patter or a circular patter. The linear pattern would result in a grid-like arrangement of pores while the circular pattern would result in pores of a fixed distance from the center of the cylinder model. The top view of the axial pore patterns can be seen in Figure 16 below.

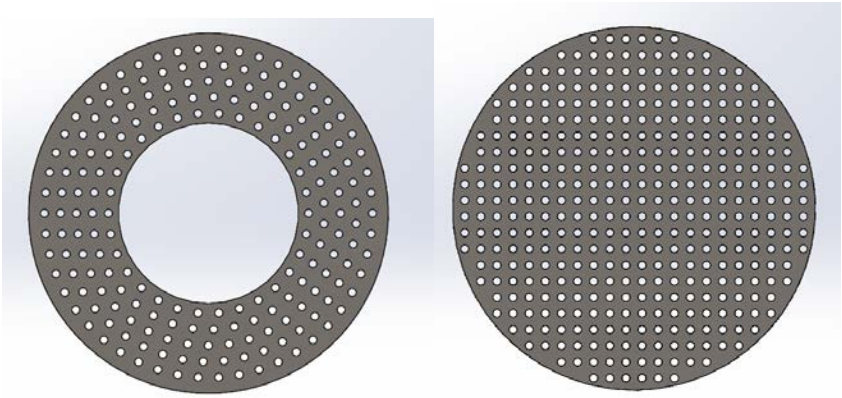

Figure 16: Shows circularly patterned pores and linearly patterned pores

It should be noted that the medullary cavity is shelled in the design on the right for Figure 16 while the medullary cavity was an extrude cut through the entire model for the design on the left. Based on the simulations and the elastic modulus calculations, the linearly applied pores are a better option at minimizing the elastic modulus than the circularly applied pores. This is because the number of pores per square inch is higher when the pores are applied linearly than circularly. As a result more pores can be applied in a smaller area, thus increasing the porosity of the implant. As porosity increases, the effective elastic modulus decreases. This relationship is further discussed in the next section. In addition to lowering the modulus better than circularly patterned axial pores, linearly applied axial pores also allow for the transversely applied pores to match up with the cuts of the axial pores. Because the transverse pores are applied in a linear manner, due to the geometry and curved edges of the model, the columns of the transverse pores can line up with the rows of the axial pores. This allows for an overall higher porosity

and allows for SolidWorks to generate a working mesh and thus a working simulation. In some cases, circularly applied axial pores cause an error in SolidWorks called 'zero-dimension geometry.' This error is associated with the geometric layout of the cuts between the axial pores and the transverse pores. When lining up the two pore patterns using a linear pattern, this error is eliminated, providing further support for the linear pattern over the circular pattern.

Porosity

Porosity is a representation of the empty space in a given design. As more pores are applied to the implant, more empty space is created and the porosity for the femur implant increases. Consequently, there is a direct relationship between the number of pores and porosity. Likewise, as porosity varies, the effective elastic modulus varies. This is because as the empty space is changed through the applications of pores, the displacement of the implant changes when forces are applied to the implant. With a higher porosity, the resultant displacements will increase given constant forces. As a result, the relationship between stress and strain changes, and thus the elastic modulus changes. With a higher strain, the modulus will decrease. The porosity of different designs was plotted in Figure 17 to better understand the relationship porosity has on the effective elastic modulus.

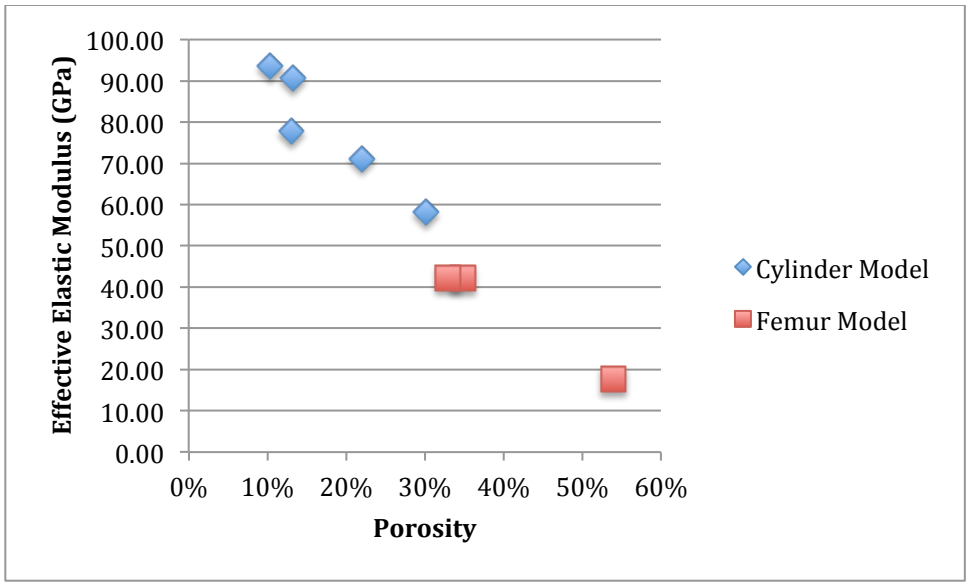

Figure 17: Shows the relationship between porosity and effective elastic modulus for various models.

There is an inverse relationship between these two properties; as the porosity of the implant increases, the modulus of the implant decreases. From this, it becomes clear that porosity between 50%-60% would yield a desired modulus between 10-20 GPa. Any design with a porosity above this may lead to a design with too small of a modulus.

Final Implant Design

After accumulating all the results from dozens of previous models, a final femur implant was designed. The final design has a height of 5.6 cm, with 1.5 mm caps on the top and bottom. The average outside radius of the implant is approximately 3.0 cm while the inside diameter, modeling the medullary cavity, is 1.6 cm. The final implant design can be seen below in Figure 18.

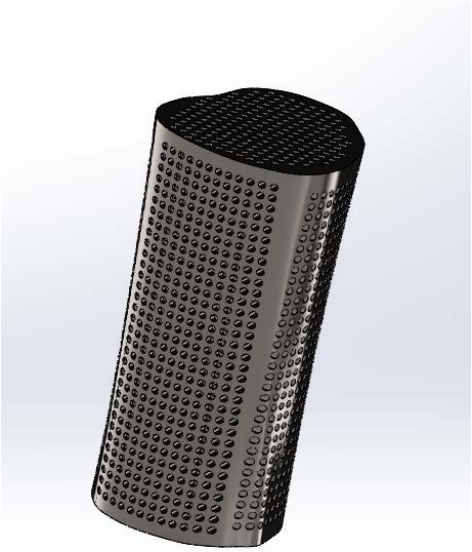

Figure 18: Shows the final design of the femur implant.

Utilizing circular pores, due to the smaller stress concentrations, pores were applied both axially and transversely. The linear pattern for the axial pores allowed the pores to align with the transversely applied pores. As a result, all the transversely applied pores connect with the axially applied pores, which provides a pathway for bone to grow throughout the implant. The top view of the implant can be seen in Figure 19 below.

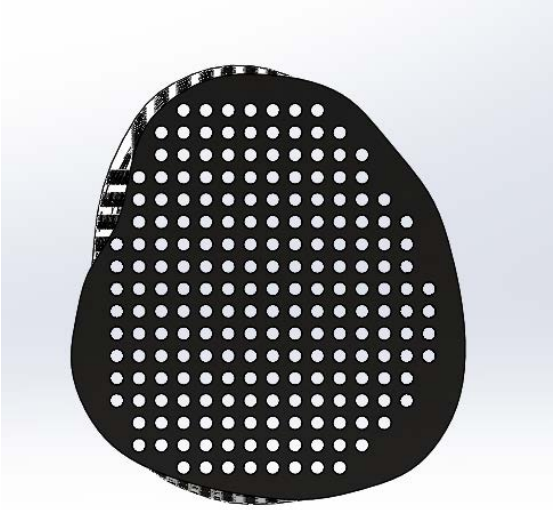

Figure 19: Shows the top view of the final design of the femur implant.

When measuring displacement in SolidWorks, several points on the top plant of the implant were probed to provide an accurate displacement measurement. The strain was calculated over a range of applied forces from 300N to 1200N. From this data, the effective elastic modulus was calculated. The results of the SolidWorks simulations have been summarized below in Table 2.

Table 2: Summarizes the final design results from simulations.

	Force Applied (N)	Stress (kPa)	Displacement (µm)	Microstrain	Elastic Modulus (GPa)
Femur18	300	458	1.25	22.4	**17.58**
	600	916	2.65	47.4	
	900	1832	4.12	73.6	
	1200	3664	5.63	100.0	

This design had an overall porosity of 54% and effective elastic modulus of 17.58 GPa. This modulus, within the range of bone's modulus, will aid in osseointegration because it will behave mechanically similar to the femur.

Calculation of the Modulus

Utilizing Equation 5, 6, and 7, the modulus was calculated for the implant. The values of the pore geometric factor and volume fraction of porosity varied between the SolidWorks model and the manufactured implant. The pore geometric factor for the SolidWorks model was 0.0031416 with a volume fraction of porosity of 0.54 compared to the manufactured implant, which had vales of 0.0026327 and 0.552, respectively. Based on these differences, two values of the global elastic modulus were calculated: the theoretical modulus and the actual modulus. The theoretical modulus was found to be 0.140 GPa while the actual modulus was found to be 0.109 GPa. These differences in

moduli compared to the finite element analysis prediction of the implant's modulus are discussed later in the report.

Pore Characterization

When taking a closer look at the pores, it is clear that the pores are not perfect circles. Upon measuring 45 pores, across all the three planes, it was found that the pores did not match the desired dimensions. The pores did not have a 1.0 mm diameter or an area of 0.785 mm^2. During the manufacturing, the pores shrunk in size, which was anticipated. The average diameter was approximately 0.838 mm, a reduction of 16.2% compared to the SolidWorks model as a result of the fabrication process. Due to the printing process and the layering of the titanium alloy, there were imperfections. As seen in previously in Figure 10, the pores were not perfect circles, but rather jagged and inconsistent. Having a decrease in the size of the pores will directly affect the mechanical properties of the overall implant. The pores were also inconsistence between planes. The pores applied transversely were smaller in area and less circular compared to the pores applied axially. This could be due to the layering process and the direction in which the implant was printed.

The DMLS printer used for the manufacturing of this implant had a layer thickness of 60 μm. It is possible that because of this resolution and surface roughness of 125-215 RA, that the complex geometry and pattern of the pores was difficult to match using a 3D printer. 15 pores from each plane were analyzed and measured. As seen in Figure 20 below, the axial plane (1) has a smaller variability of pore size than the coronal plane (2) and the sagittal plane (3).

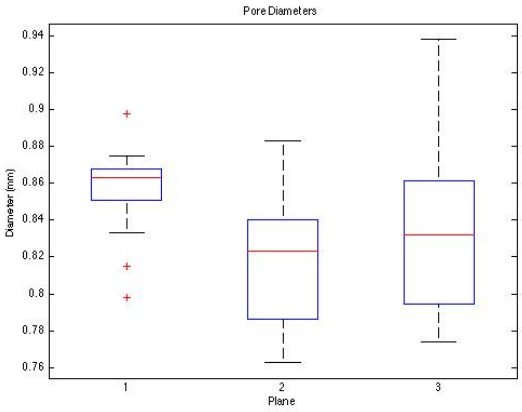

Figure 20: Box and whisker plot of the pores across three planes.

The tighter box of the axial plane represents more consistent pores on that specific plane compared to the box and whisker plots of the coronal plane and the sagittal plane. The specific measurements of the pores can be found in Appendix IV.

Additionally, analysis of variance was performed on the three planes of pores. Analysis of variance (ANOVA) is a statistical model that is used to analyze the differences between experimental groups. Using ANOVA for the analysis of the pores, the p-value can be determined which provides important statistical information concerning the variation of pores. P-values greater than 0.05 demonstrates a weak or non-existence of variation between different sets of data while p-values less than 0.05 demonstrates a strong existence of variation. It was determined that the p-level was 0.038. Because this value is smaller than 0.05, there is significant difference between the pores across different planes[18].

Table 3: Shows the ANOVA results for the different planes of the femur implant.

Analysis of Variance (One-Way)

Summary

Groups	*Sample size*	*Sum*	*Mean*	*Variance*
Axial	15	12.842	0.85613	0.00061
Coronal	15	12.305	0.82033	0.00116
Sagitall	15	12.524	0.83493	0.00236

ANOVA

Source of Variation	*SS*	*df*	*MS*	*F*	*p-level*	*F crit*
Between Groups	0.00972	2	0.00486	3.53009	0.03828	4.30012
Within Groups	0.05783	42	0.00138			
Total	0.06755	44				

Because of these differences among pores on different planes, the mechanical properties of the implant as a whole will not match the mechanical properties of the SolidWorks design. Also, this variance displays some issues concerning the manufacturing of similar implants using direct metal laser sintering 3D printers. Information about these differences in pores should be considered in the implant's design prior to printing in future studies. For the complete analysis of variance on the pore geometry, see Appendix V.

Comparison between Theoretical Implant and Actual Implant

The femur implant was examined post printing. Figure 21 below shows a side-by-side comparison of the two implants. Initially, it appears that the two femur implants are nearly identical.

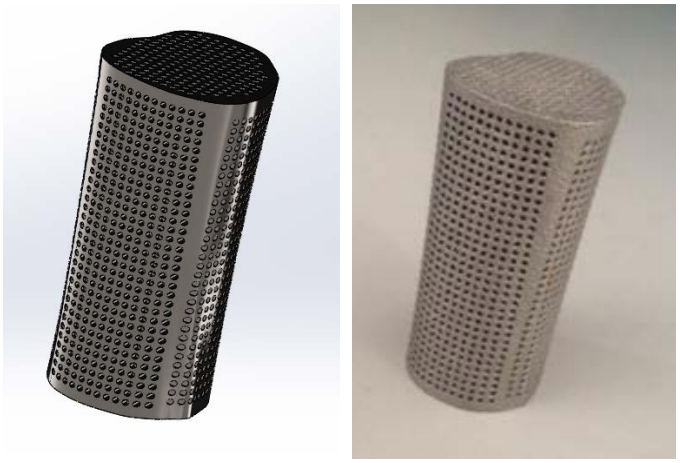

Figure 21: Shows a side-by-side comparison between the theoretical implant and the actual implant

Using calipers, the height was measured to be 5.65 cm, compared to the theoretical value of 5.6 cm. This discrepancy may be due to the expanding material during the printing process, a side effect that was also responsible for the pore diameter shrinkage. Using an electronic scale, the mass was measured to be 59.6 grams. To measure the volume of the implant, a graduated cylinder was used. The cylinder, which had a diameter only slightly larger than the implant, was filled with water of a known volume. The implant was placed in the graduated cylinder and water was displaced. Allowing ample time for the air bubbles inside the pores of the implant to vent to the surface of the cylinder, the new volume inside the cylinder was measured. The difference between the two measurements was used as the volume of the implant and was calculated to be 16.0 cm^3.

From the mass and volume of the implant, the density of the implant was calculated to be 3.73 g/cm^3, a percent difference of -15.8% compared to the computer model. These differences of the implant's characteristics between the theoretical design and the actual design have direct implications on the properties of the femur implant. Additionally, the porosity was measured using the computer value for the volume of the implant without the pores and without the medullary cavity. Using this value and the

measured value of the volume, the implant porosity was calculated to be 55.2%. This value was much closer to the theoretical value of porosity of 54% based on the SolidWorks model. A summary of the measurements for both the theoretical implant and the actual implant can be seen below in Table 4.

Table 4: Summarizes measurements of the implant compared to the theoretical dimensions.

	Theoretical Implant	Actual Implant	Percent Difference
Mass (g)	59.2	59.6	0.7%
Volume (cm^3)	13.37	16	19.7%
Density (g/cm^3)	4.43	3.73	-15.8%
Porosity	54.0%	55.2%	2.2%

As mentioned in the previous section, the pore geometry varied between the theoretical model and the printed model. However, in addition to these variations in pore shape and pore size, there was also a crack that was present on the printed model. Due to the pore pattern of the implant and the limitations of the layering resolution provided by the manufacturing, a crack measuring approximately 2.0 cm was created. This crack had minor influence on the mechanical properties of the implant, specifically pertaining to the elastic modulus. A model of the defect was recreated in SolidWorks and compressive loads were applied to better understand the impact this defect had on the effective elastic modulus of the implant. The pore that caused the crack was increased in diameter to 1.25 mm. At this dimension, the crack that resulted in the SolidWorks model matches the crack in the actual implant very closely. This model can be seen below in Figure 22.

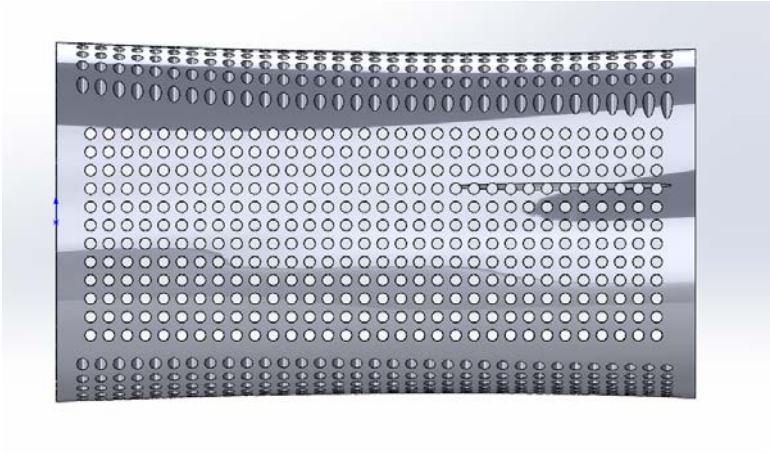

Figure X: Shows the SolidWorks recreation of the implant crack.

It was found that the resulting modulus was 16.45 GPa, a percent difference of -6.43%. Consequently, this crack had a minimal effect on the modulus of the implant. The defect on the actual implant can be better seen in Figure 23 below.

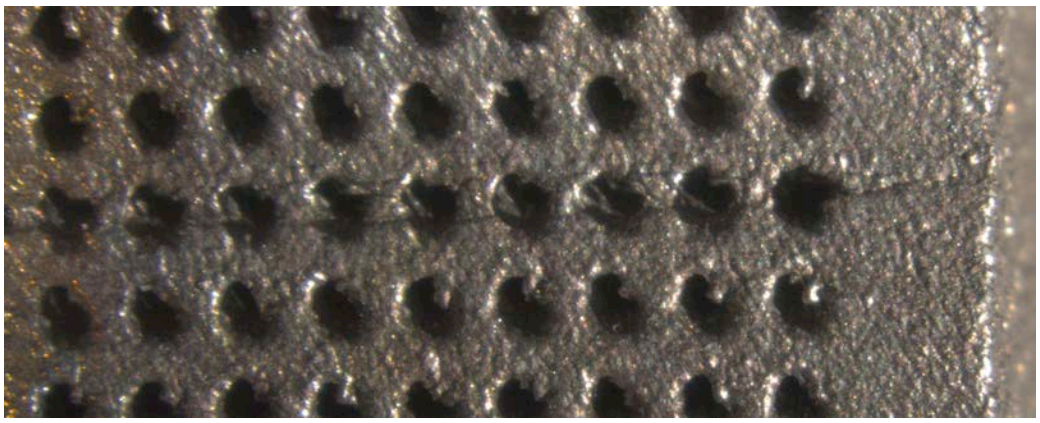

Figure 23: Shows the crack length and orientation on the femur implant.

Upon a closer view of the crack, it becomes apparent that the crack has caused some pores to connect with surrounding pores. This will affect the load distributions on the implant upon compression tests and will result in higher stress concentrations around the pores that are affected by the crack. Figure 24 below is a close-up view of the pores near the crack.

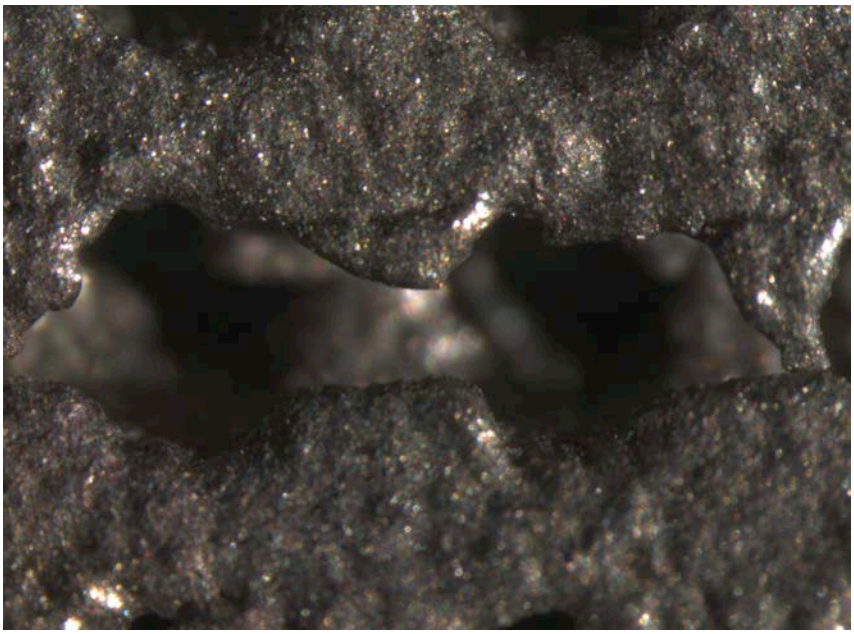

Figure 24: Shows connected pores, resulting from the crack on the implant.

Based on these measurements and differences between dimensions of the theoretical implant and the actual implant, the elastic modulus will vary. As a result, implant will behave mechanically different from the finite element analysis, which was performed on the theoretical design of the implant. With the large volume increase, resulting in a decrease in density by 16%, the elastic modulus is predicted to decrease. Despite the decease of pore size by 17%, which would mean there would be more material and thus a higher stiffness, the decrease in density is believed to have a greater impact on the elastic modulus compared to the pore size. To calculate the global elastic modulus of the implant, compression tests were done to verify the hypothesis that the elastic modulus will be smaller in value compared to the theoretical modulus.

Compression Tests

As previously discussed, several compressive loads were applied to the implant and an extensometer was used to measure strain. A compressive load of 600N was

applied to the implant on 4 separate tests, using the cross sectional area of 0.655 mm^2 for the calculation of stress. The resulting stress versus strain curves can be seen in Figure 25 below.

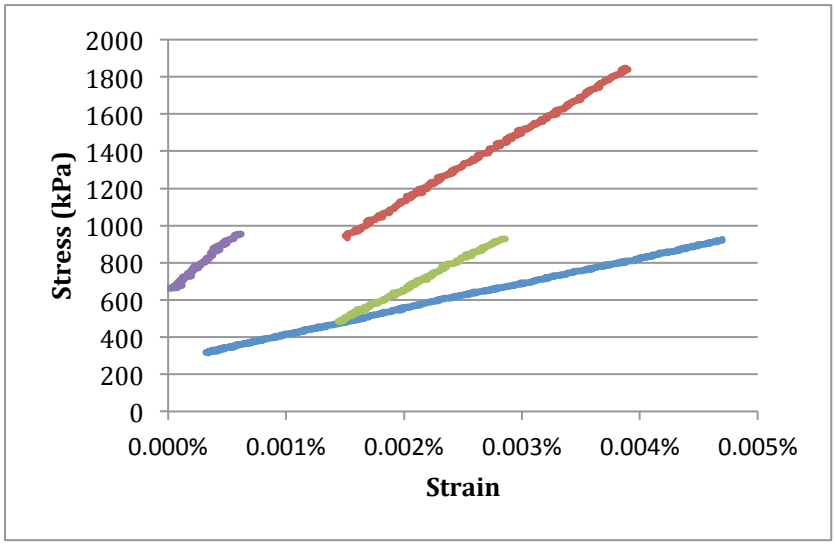

Figure 25: Shows the stress and strain curves for the four 600N-compression trials.

During the trials, there were disruptive side effects of the strain due to the compliance of the tensile testing machine. As a result, the first 20%-25% of the load and displacement data was removed from the graph to provide a more accurate representation of the relationship between the stress and strain for the femur implant.

Compressive loads of 1200N were also applied to the implant. This loading was chosen because it represents the compressive loading that the implant would experience if the patient were standing on one leg. The results of these four trials can be seen in Figure 26 below.

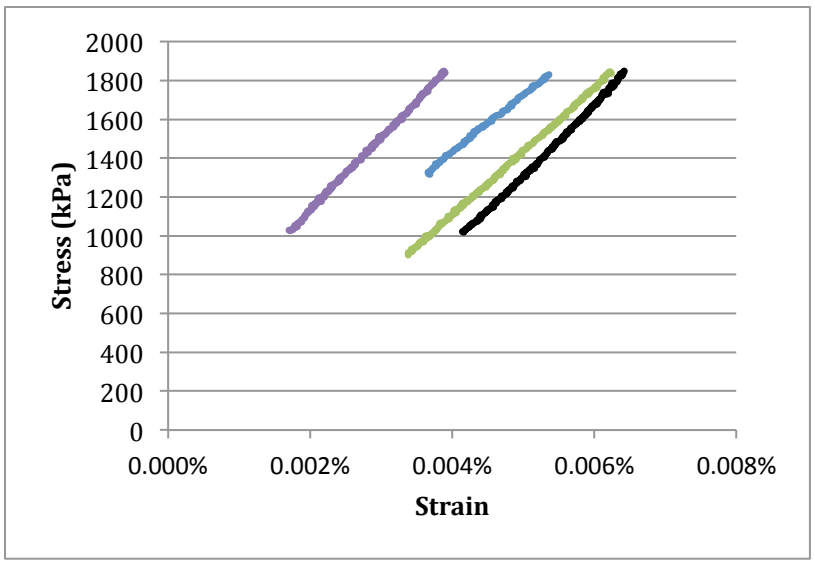

Figure 26: Shows the stress and strain curves for the four 1200N-compression trials.

As was done for the 600N trials, the first 20%-25% of the data was removed to eliminate a variable slope due to machine compliance and thus giving a more accurate measurement of the elastic modulus for the implant. While strain was measured using an extensometer for all eight trials, the crosshead displacement of the tension machine was also measured. However, due to the inaccuracies in the measurement of crosshead displacement these data values were not used.

The slopes of the 600N trials were measured and averaged to provide a value for the global elastic modulus of the implant. This value was 0.690 GPa. The same was done for the 1200N trials, which determined the elastic modulus of the implant was 0.688 GPa. The complete experimental data can be seen below in Table 5.

Table 5: Shows the experimental results from the compression tests.

Sample	Load	Elastic Modulus (GPa)
01	600N	0.283
04	600N	0.753
06	600N	0.647
08	600N	1.076
03	1200N	0.619
05	1200N	0.728
07	1200N	0.654
09	1200N	0.749

The standard deviation of these trials is 0.203 GPa. The agreements between the eight compression trials ensure that this measured value of the elastic modulus is repeatable and thus an accurate representation of the material property for the manufactured femur implant.

CONCLUSION:

Conflicting Elastic Moduli Results

Through the various methods and procedures to calculate and measure the elastic modulus of the designed femur implant several conflicting results were obtained. These various methods and their results are summarized below in Table 6.

Table 6: Shows the calculated and measured values of the elastic moduli.

Global Elastic Modulus		
Ti-6Al-4V Alloy	118.0	GPa
Finite Element Analysis	17.58	GPa
Equation (7) - Theoretical	0.140	GPa
Equation (7) - Actual	0.109	GPa
Extensometer - 600N	0.690	GPa
Extensometer - 1200N	0.688	GPa

While Ti-6Al-4V alloy has an elastic modulus of 118.0 GPa, it is imperative to get the implant's elastic modulus to a value much closer to the modulus of bone, which ranges between 10 – 20 GPa. Two methods were used to predict the elastic modulus before testing the final implant. The alternative equation and the finite element analysis yielded very different results. The equation used was based on empirical data on similarly porous medical implants[19]. This equation provided an approximation that was much closer to the actual elastic modulus of the implant compared to finite element analysis. Finite element analysis has limitations, especially concerning porous parts. This is in part due to how SolidWorks models the implant. While finite element analysis is an accurate and effective way to model structures, the pores in the implant are difficult to model. Consequently, finite element analysis is only partially effective because of the modeling of the pores.

Additionally, the printed femur had differences compared to the SolidWorks design, which were partially responsible for the differences in the elastic modulus. The printed femur had a decrease in density, potentially because the material that was layered for the printing process was not the desired 99% dense. The decrease in density and increase in the volume of the implant cause the elastic modulus of the implant to be lower compared to the expected value from finite element analysis. There are other methods of analysis that may prove more precise in predicting the effective elastic modulus of the printed medical implant.

In the future, a more accurate micromechanics approach could be taken to better predict the elastic modulus of medical implants. One such method that could be further explored is the composite cylindrical assemblage method.

Composite Cylindrical Assemblage

Composite cylindrical assemblage is a specific method to analyze and model complex composite materials[20]. Treating the pores as air, this model could be applied to better understand the global mechanical properties of the femur implant. A general model of this subsection of micromechanics can be seen in Figure 27 below.

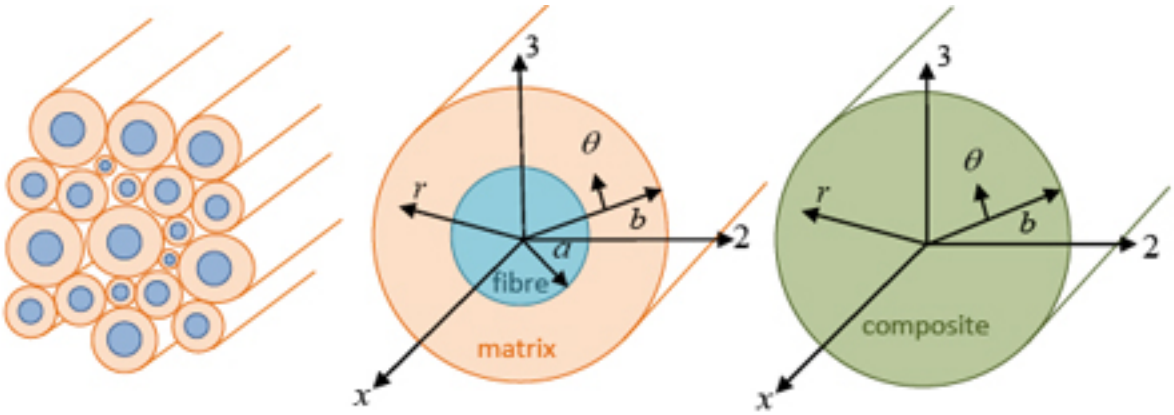

Figure 27: Shows the modeling of complex composite cylinders[21].

One advantage of the composite cylindrical assemblage model is that this model is sufficient in determining the elastic modulus of transversely isotropic parts, which is relevant to the femur implant that was modeled.

3D Printing

While direct metal laser sintering printer (DMLS) was used for the manufacturing of this implant, there are other 3D printer options that were considered. Electron beam melting (EBM) is another additive manufacturing printer for metal parts. EBM prints parts by the melting of metal powder layer by layer by an electron beam in a vacuum. Both DMLS and EBM were considered and compared for the manufacturing of the femur implant. DMLS printers have a better layer thickness, on average, of 20 – 40 μm compared to EBM, which has a layer thickness of 50 – 70 μm[22]. While both printers

work for the desired titanium allow, DMLS has a better surface finish and dimensional accuracy for Ti-6Al-4V compared to EBM. Additionally, printing quotes were consistently lower for DMLS providers compared to EBM providers. EBM parts generally have lower residual stressed compared to DMLS parts; despite this, DMLS was chosen for its superior dimensional accuracies and tolerances.

Future Work

The femur implant that was designed had defects that were not desirable. If direct metal laser sintering 3D printer is a manufacturing option that is pursued in the future, the corresponding model that is to be printed must be adjusted to account for shrinkage and a reduction in mechanical properties.

Figure 28: Shows a direct metal laser sintering (DMLS) 3D printer.

Because the pores decreased in area after the printing process, the pores need to be designed to a larger size so after the material expands, the pores would be the appropriate size. Based on the pores shrinking by 16.2% on the model that was printed, future models should incorporate pores that are approximately 1.19 mm in diameter instead of 1.00 mm. Should the pores shrink, as they did previously, the end pore size

would be the originally desired size. Additionally, the pore that was the cause of the crack in the implant should be removed. The specific pore was approximately 49 μm away from the wall of the femur implant. This distance was too small; the printer could not reach the necessary tolerance to print the model as the SolidWorks design specified. However, it cannot be determined if the manufacturing of the implant was an anomaly as only one implant was printed. A larger sample size is required to better understand the 3D printing of patient specific implants. Thus, DLMS printing should continue to be utilized for the manufacturing of future medical implants.

To avoid similar issues that were encountered printing the implant, a different computer aided design program could be used. Within Medical, a program that is used to design medical implants of a similar nature to this project is a potential solution. This program has the ability to create porous implants and is suited for DMLS manufacturing. This program can aid in the elimination of errors such as complex geometry that is not printable. One limitation of this program is that finite element analysis cannot be performed within the program. While finite element analysis is a critical component in the design process, alternative solutions could be explored to allow the design to be created in the Within Medical technology and exported to SolidWorks for analysis.

The SolidWorks femur implant was not modeled with screws and a brace. During the surgical procedure where the femur implant would be inserted into the patient, the surgeon would secure the implant with several medical screws and a brace on the lateral side of the femur. This brace provides support on the tension side of the femur because bone acts better in compression than tension. In order to better understand the stresses in the implant, it is important to model these screws and braces in finite element analysis.

For future work, these features could be implemented in the design and analysis of creating an optimized femur implant.

Lastly, while moment forces were modeling in SolidWorks, these compression forces were not replicated during mechanical testing of the 3D printed model. To verify experimental results, these moment forces should be applied to the implant in a controlled and repeatable manner. Testing the implant in this manner would provide crucial information on how the implant may react under life-like conditions that would be experienced through activities of the patient.

Impact on the Medical Field

With the limitations of current treatments for bone cancer, a better solution is necessary. Creating custom, patient specific implants, has the potential to remedy this problem and create a large impact on the medical field. With the advancement of technology and 3D printing, patient specific implants is a realistic option and needs to be further investigated. Direct metal laser sintering 3D printing has been a primary focus on the printing of porous implants. This printer creates a slightly rough surface of the part being printed. This roughness is very beneficial for bone attachment because the rough surface has a higher surface area compared to smooth surface. A porous implant, with mechanical properties similar to bone will promote bone growth and osseointegration. By allowing bone to grow into and throughout the implant, the implant will be more securely placed in the patient and loosening and failure will decrease as a direct result. By having a longer implant life, less corrective surgeries are necessary and patient discomfort will decrease. These developments are the future for bone cancer treatments.

APPENDIX:

Appendix I: Preliminary Cylinder-Model Results

	Cylinder Model							Results				
	Diameter	Inner D	Height	Pore Size	Pore Pattern			Force Applied (N)	Area	Stress (Pa)	Displacement	Strain	Elastic Modulus
					Shape	Radial	X/Y						
1	0.04500	0.02225	0.05000	0.0010	Circles	None	X/Y	300	0.00120161	249665.0114	1.97E-06	1.97E-06	98.0 GPa
	0.04500	0.02225	0.05000	0.0010	Circles	None	X/Y	600	0.00120161	499330.0229	4.08E-06	4.08E-06	
	0.04500	0.02225	0.05000	0.0010	Circles	None	X/Y	900	0.00120161	748995.0343	6.97E-06	6.97E-06	
	0.045	0.02225	0.05	0.001	Circles	None	X/Y	1200	0.00120161	998660.0457	8.66E-06	8.66E-06	
2	0.04500	0.02225	0.05000	0.0010	Squares	Three Rows	None	300	0.00120161	249665.0114	1.27E-07	2.53E-06	98.2 GPa
	0.04500	0.02225	0.05000	0.0010	Squares	Three Rows	None	600	0.00120161	499330.0229	2.53E-07	5.06E-06	
	0.04500	0.02225	0.05000	0.0010	Squares	Three Rows	None	900	0.00120161	748995.0343	3.79E-07	7.59E-06	
	0.04500	0.02225	0.05000	0.0010	Squares	Three Rows	None	1200	0.00120161	998660.0457	5.06E-07	1.01E-05	
3	0.04500	0.02225	0.05000	0.0010	Triangle	Three Rows	None	300	0.00120161	249665.0114	1.26E-07	2.52E-06	98.5 GPa
	0.04500	0.02225	0.05000	0.0010	Triangle	Three Rows	None	600	0.00120161	499330.0229	2.51E-07	5.05E-06	
	0.04500	0.02225	0.05000	0.0010	Triangle	Three Rows	None	900	0.00120161	748995.0343	3.76E-07	7.57E-06	
	0.04500	0.02225	0.05000	0.0010	Triangle	Three Rows	None	1200	0.00120161	998660.0457	5.02E-07	1.01E-05	
Radial and XY	0.04500	0.02225	0.05000	0.0010	Circles	Three Rows	None	300	0.00120161	249665.0114	1.60E-07	3.21E-06	77.8 GPa
	0.04500	0.02225	0.05000	0.0010	Circles	Three Rows	None	600	0.00120161	499330.0229	3.21E-07	6.42E-06	
	0.04500	0.02225	0.05000	0.0010	Circles	Three Rows	None	900	0.00120161	748995.0343	4.81E-07	9.63E-06	
	0.04500	0.02225	0.05000	0.0010	Circles	Three Rows	None	1200	0.00120161	998660.0457	6.42E-07	1.28E-05	

Appendix II: Advanced Cylinder-Model Results

	Optimized Axial								Results				
				Pore Pattern									
	Diameter	Inner D	Height	Pore Size	Shape	Radial	Numbers	X/Y	Force Applied (N)	Area (m2)	Stress (Pa)	Displacement	Strain	Elastic Modulus
OA1	0.04500	0.02225	0.05000	0.00100	Circles	5 Rows	30, 35, 40, 45, 50	None	300	0.00120161	249665.011	-1.38E-07	-2.75E-06	90.7 MPa
	0.04500	0.02225	0.05000	0.00100	Circles	5 Rows	30, 35, 40, 45, 50	None	600	0.00120161	499330.023	-2.75E-07	-5.50E-06	
	0.04500	0.02225	0.05000	0.00100	Circles	5 Rows	30, 35, 40, 45, 50	None	900	0.00120161	748995.034	-4.13E-07	-8.25E-06	
	0.04500	0.02225	0.05000	0.00100	Circles	5 Rows	30, 35, 40, 45, 50	None	1200	0.00120161	998660.046	-5.50E-07	-1.10E-05	
OA2	0.04500	0.02225	0.05000	0.00075	Squares	6 Rows	35-40-45-50-55-60	None	300	0.00120161	249665.011	-1.33E-07	-2.664E-06	93.7 MPa
	0.04500	0.02225	0.05000	0.00075	Squares	6 Rows	35-40-45-50-55-61	None	600	0.00120161	499330.023	-2.66E-07	-5.33E-06	
	0.04500	0.02225	0.05000	0.00075	Squares	6 Rows	35-40-45-50-55-62	None	900	0.00120161	748995.034	-4.00E-07	-7.99E-06	
	0.04500	0.02225	0.05000	0.00075	Squares	6 Rows	35-40-45-50-55-63	None	1200	0.00120161	998660.046	-5.33E-07	-1.07E-05	
OA3	0.04500	0.02225	0.05000	0.00100	Triangle	5 Rows	30, 35, 40, 45, 50	X and Y	300	0.00120161	249665.011	-2.52E-07	-5.04E-06	49.5 MPa
	0.04500	0.02225	0.05000	0.00100	Triangle	5 Rows	30, 35, 40, 45, 50	X and Y	600	0.00120161	499330.023	-5.04E-07	-1.01E-05	
	0.04500	0.02225	0.05000	0.00100	Triangle	5 Rows	30, 35, 40, 45, 50	X and Y	900	0.00120161	748995.034	-7.56E-07	-1.51E-05	
	0.04500	0.02225	0.05000	0.00100	Triangle	5 Rows	30, 35, 40, 45, 50	X and Y	1200	0.00120161	998660.046	-1.01E-06	-2.02E-05	
OA4	0.04500	0.02225	0.05000	0.00100	Triangle	5 Rows	30, 35, 40, 45, 50, 55, 60	Three Planes	300	0.00120161	249665.011	-2.15E-07	-4.29E-06	58.2 MPa
	0.04500	0.02225	0.05000	0.00100	Triangle	5 Rows	30, 35, 40, 45, 50, 55, 60	Three Planes	600	0.00120161	499330.023	-4.29E-07	-8.58E-06	
	0.04500	0.02225	0.05000	0.00100	Triangle	5 Rows	30, 35, 40, 45, 50, 55, 60	Three Planes	900	0.00120161	748995.034	-6.44E-07	-1.29E-05	
	0.04500	0.02225	0.05000	0.00100	Triangle	5 Rows	30, 35, 40, 45, 50, 55, 60	Three Planes	1200	0.00120161	998660.046	-8.58E-07	-1.72E-05	
SO1	0.04500	0.02250	0.05600	0.00100	Circles	2 mm Spacing	Linear Pattern	Three Planes	300	0.00119282	251504.108	1.12E-06	2.01E-05	12.55 GPa
	0.04500	0.02250	0.05600	0.00100	Circles	2 mm Spacing	Linear Pattern	Three Planes	600	0.00119282	503008.215	2.25E-06	4.01E-05	
	0.04500	0.02250	0.05600	0.00100	Circles	2 mm Spacing	Linear Pattern	Three Planes	900	0.00119282	754512.323	3.37E-06	6.01E-05	
	0.04500	0.02250	0.05600	0.00100	Circles	2 mm Spacing	Linear Pattern	Three Planes	1200	0.00119282	1006016.43	4.49E-06	8.02E-05	

Appendix III: Femur-Model Results

	Optimized Axial								Results				
				Pore Pattern				Force				
	Diameter	Inner D	Height	Pore Size	Shape	Radial	Numbers	X/Y	Applied (N)	Area (m2)	Stress (Pa)	Disp	Strain	Elastic Modulus
Femur1	0.03000	0.00000	0.05600	0.00100	Circles	2 mm Spacing	Linear Pattern	Three Planes	300	0.00070686	424413.182	5.63E-07	1.01E-05	42.20 GPa
	0.03000	0.00000	0.05600	0.00100	Circles	2 mm Spacing	Linear Pattern	Three Planes	600	0.00070686	848826.363	1.13E-06	2.01E-05	
	0.03000	0.00000	0.05600	0.00100	Circles	2 mm Spacing	Linear Pattern	Three Planes	900	0.00070686	1273239.54	1.69E-06	3.02E-05	
	0.03000	0.00000	0.05600	0.00100	Circles	2 mm Spacing	Linear Pattern	Three Planes	1200	0.00070686	1697652.73	2.25E-06	4.02E-05	
Femur2	0.03000	0.01250	0.05600	0.00100	Circles	2 mm Spacing	Linear Pattern	Three Planes	300	0.000655	458015.267	6.79E-07	1.21E-05	37.76 GPa
	0.03000	0.01250	0.05600	0.00100	Circles	2 mm Spacing	Linear Pattern	Three Planes	600	0.000655	916030.534	1.36E-06	2.43E-05	
	0.03000	0.01250	0.05600	0.00100	Circles	2 mm Spacing	Linear Pattern	Three Planes	900	0.000655	1374045.8	2.04E-06	3.64E-05	
	0.03000	0.01250	0.05600	0.00100	Circles	2 mm Spacing	Linear Pattern	Three Planes	1200	0.000655	1832061.07	2.72E-06	4.85E-05	
Femur3	0.03000	0.01250	0.05600	0.00100	Circles	2 mm Spacing	Linear Pattern	Three Planes	300	0.000655	458015.267	1.19E-06	2.12E-05	21.63 GPa
	0.03000	0.01250	0.05600	0.00100	Circles	2 mm Spacing	Linear Pattern	Three Planes	600	0.000655	916030.534	2.37E-06	4.23E-05	
	0.03000	0.01250	0.05600	0.00100	Circles	2 mm Spacing	Linear Pattern	Three Planes	900	0.000655	1374045.8	3.56E-06	6.36E-05	
	0.03000	0.01250	0.05600	0.00100	Circles	2 mm Spacing	Linear Pattern	Three Planes	1200	0.000655	1832061.07	4.74E-06	8.47E-05	
Femur4	0.03000	0.01250	0.05600	0.00100	Circles	2 mm Spacing	Linear Pattern	Three Planes	300	0.000655	458015.267	3.13E-06	5.59E-05	8.19 GPa
	0.03000	0.01250	0.05600	0.00100	Circles	2 mm Spacing	Linear Pattern	Three Planes	600	0.000655	916030.534	6.26E-06	1.12E-04	
	0.03000	0.01250	0.05600	0.00100	Circles	2 mm Spacing	Linear Pattern	Three Planes	900	0.000655	1374045.8	9.40E-06	1.68E-04	
	0.03000	0.01250	0.05600	0.00100	Circles	2 mm Spacing	Linear Pattern	Three Planes	1200	0.000655	1832061.07	1.25E-05	2.24E-04	
Femur5	0.03000	0.01250	0.05600	0.00100	Circles	2 mm Spacing	Linear Pattern	Three Planes	300	0.000655	458015.267	3.27E-06	5.84E-05	7.84 GPa
	0.03000	0.01250	0.05600	0.00100	Circles	2 mm Spacing	Linear Pattern	Three Planes	600	0.000655	916030.534	6.55E-06	1.17E-04	
	0.03000	0.01250	0.05600	0.00100	Circles	2 mm Spacing	Linear Pattern	Three Planes	900	0.000655	1374045.8	9.82E-06	1.75E-04	
	0.03000	0.01250	0.05600	0.00100	Circles	2 mm Spacing	Linear Pattern	Three Planes	1200	0.000655	1832061.07	1.31E-05	2.34E-04	
Femur6	0.03000	0.01250	0.05600	0.00100	Circles	2 mm Spacing	Linear Pattern	Three Planes	300	0.000655	458015.267	1.26E-06	2.25E-05	20.38 GPa
	0.03000	0.01250	0.05600	0.00100	Circles	2 mm Spacing	Linear Pattern	Three Planes	600	0.000655	916030.534	2.52E-06	4.49E-05	
	0.03000	0.01250	0.05600	0.00100	Circles	2 mm Spacing	Linear Pattern	Three Planes	900	0.000655	1374045.8	--	--	
	0.03000	0.01250	0.05600	0.00100	Circles	2 mm Spacing	Linear Pattern	Three Planes	1200	0.000655	1832061.07	--	--	
Femur7	0.03000	0.01250	0.05600	0.00100	Circles	2 mm Spacing	Linear Pattern	Three Planes	300	0.000655	458015.267	1.71E-06	3.06E-05	**14.99 GPa**
	0.03000	0.01250	0.05600	0.00100	Circles	2 mm Spacing	Linear Pattern	Three Planes	600	0.000655	916030.534	3.42E-06	6.11E-05	
	0.03000	0.01250	0.05600	0.00100	Circles	2 mm Spacing	Linear Pattern	Three Planes	900	0.000655	1374045.8	5.13E-06	9.17E-05	
	0.03000	0.01250	0.05600	0.00100	Circles	2 mm Spacing	Linear Pattern	Three Planes	1200	0.000655	1832061.07	6.85E-06	1.22E-04	
Femur7, Revisited	0.03000	0.01250	0.05600	0.00100	Circles	2 mm Spacing	Linear Pattern	Three Planes	300	0.000655	458015.267	7.61E-07	1.36E-05	**33.82 GPa**
	0.03000	0.01250	0.05600	0.00100	Circles	2 mm Spacing	Linear Pattern	Three Planes	600	0.000655	916030.534	1.53E-06	2.74E-05	
	0.03000	0.01250	0.05600	0.00100	Circles	2 mm Spacing	Linear Pattern	Three Planes	900	0.000655	1374045.8	2.29E-06	4.09E-05	
	0.03000	0.01250	0.05600	0.00100	Circles	2 mm Spacing	Linear Pattern	Three Planes	1200	0.000655	1832061.07	3.04E-06	5.42E-05	
Femur7, Localized Force	0.03000	0.01250	0.05600	0.00100	Circles	2 mm Spacing	Linear Pattern	Three Planes	300	0.000655	458015.267	7.33E-07	1.31E-05	**35.00 GPa**
	0.03000	0.01250	0.05600	0.00100	Circles	2 mm Spacing	Linear Pattern	Three Planes	600	0.000655	916030.534	1.47E-06	2.62E-05	
	0.03000	0.01250	0.05600	0.00100	Circles	2 mm Spacing	Linear Pattern	Three Planes	900	0.000655	1374045.8	2.20E-06	3.93E-05	
	0.03000	0.01250	0.05600	0.00100	Circles	2 mm Spacing	Linear Pattern	Three Planes	1200	0.000655	1832061.07	--	--	

Femur8	0.03000	0.01250	0.05600	0.00100	Circles	1.8 mm Spacing	Linear Pattern	Three Planes	300	0.000655	458015.267	9.99E-07	1.78E-05	26.09 GPa
	0.03000	0.01250	0.05600	0.00100	Circles	1.8 mm Spacing	Linear Pattern	Three Planes	600	0.000655	916030.534	1.98E-06	3.53E-05	
	0.03000	0.01250	0.05600	0.00100	Circles	1.8 mm Spacing	Linear Pattern	Three Planes	900	0.000655	1374045.8	2.97E-06	5.29E-05	
	0.03000	0.01250	0.05600	0.00100	Circles	1.8 mm Spacing	Linear Pattern	Three Planes	1200	0.000655	1832061.07	--	--	
Femur9	0.03000	0.01250	0.05600	0.00100	Circles	1.5 mm Spacing	Linear Pattern	Three Planes	300	0.000655	458015.267		0.00E+00	Won't Run
	0.03000	0.01250	0.05600	0.00100	Circles	1.5 mm Spacing	Linear Pattern	Three Planes	600	0.000655	916030.534		0.00E+00	
	0.03000	0.01250	0.05600	0.00100	Circles	1.5 mm Spacing	Linear Pattern	Three Planes	900	0.000655	1374045.8		0.00E+00	
	0.03000	0.01250	0.05600	0.00100	Circles	1.5 mm Spacing	Linear Pattern	Three Planes	1200	0.000655	1832061.07		0.00E+00	
Femur10	0.03000	0.01250	0.05600	0.00100	Circles	1.8 mm Spacing	Linear Pattern	Three Planes	300	0.000655	458015.267	8.26E-07	1.47E-05	31.07 GPa
	0.03000	0.01250	0.05600	0.00100	Circles	1.8 mm Spacing	Linear Pattern	Three Planes	600	0.000655	916030.534	1.65E-06	2.95E-05	
	0.03000	0.01250	0.05600	0.00100	Circles	1.8 mm Spacing	Linear Pattern	Three Planes	900	0.000655	1374045.8	2.48E-06	4.42E-05	
	0.03000	0.01250	0.05600	0.00100	Circles	1.8 mm Spacing	Linear Pattern	Three Planes	1200	0.000655	1832061.07	--	--	
Femur11	0.03000	0.01250	0.05600	0.00100	Circles	1.8 mm Spacing	Linear Pattern	Three Planes	300	0.000655	458015.267	7.11E-07	1.27E-05	36.09 GPa
	0.03000	0.01250	0.05600	0.00100	Circles	1.8 mm Spacing	Linear Pattern	Three Planes	600	0.000655	916030.534	1.42E-06	2.54E-05	
	0.03000	0.01250	0.05600	0.00100	Circles	1.8 mm Spacing	Linear Pattern	Three Planes	900	0.000655	1374045.8		0.00E+00	
	0.03000	0.01250	0.05600	0.00100	Circles	1.8 mm Spacing	Linear Pattern	Three Planes	1200	0.000655	1832061.07	--	--	
Femur12	0.03000	0.01250	0.05600	0.00100	Circles	1.6 mm Spacing	Linear Pattern	Three Planes	300	0.000655	458015.267	1.11E-06	1.98E-05	~24 GPa
	0.03000	0.01250	0.05600	0.00100	Circles	1.6 mm Spacing	Linear Pattern	Three Planes	600	0.000655	916030.534		0.00E+00	
	0.03000	0.01250	0.05600	0.00100	Circles	1.6 mm Spacing	Linear Pattern	Three Planes	900	0.000655	1374045.8		0.00E+00	
	0.03000	0.01250	0.05600	0.00100	Circles	1.6 mm Spacing	Linear Pattern	Three Planes	1200	0.000655	1832061.07	--	--	
Femur13	0.03000	0.01250	0.05600	0.00100	Circles	1.6 mm Spacing	Linear Pattern	Three Planes	300	0.000655	458015.267	1.15E-06	2.05E-05	22.3 Gpa/27.5 GPa
	0.03000	0.01250	0.05600	0.00100	Circles	1.6 mm Spacing	Linear Pattern	Three Planes	600	0.000655	916030.534	2.30E-06	4.11E-05	
	0.03000	0.01250	0.05600	0.00100	Circles	1.6 mm Spacing	Linear Pattern	Three Planes	900	0.000655	1374045.8	3.45E-06	6.16E-05	
	0.03000	0.01250	0.05600	0.00100	Circles	1.6 mm Spacing	Linear Pattern	Three Planes	900	0.000655	458015.267	9.33E-07	1.67E-05	
	0.03000	0.01250	0.05600	0.00100	Circles	1.6 mm Spacing	Linear Pattern	Three Planes	900	0.000655	916030.534	1.87E-06	3.34E-05	
	0.03000	0.01250	0.05600	0.00100	Circles	1.6 mm Spacing	Linear Pattern	Three Planes	900	0.000655	1374045.8	2.80E-06	5.00E-05	
Femur14	0.03000	0.01250	0.05600	0.00100	Circles	1.4 mm Spacing	Linear Pattern	Three Planes	300	0.000655	458015.267		0.00E+00	Won't Run
	0.03000	0.01250	0.05600	0.00100	Circles	1.4 mm Spacing	Linear Pattern	Three Planes	600	0.000655	916030.534		0.00E+00	
	0.03000	0.01250	0.05600	0.00100	Circles	1.4 mm Spacing	Linear Pattern	Three Planes	900	0.000655	1374045.8		0.00E+00	
	0.03000	0.01250	0.05600	0.00100	Circles	1.4 mm Spacing	Linear Pattern	Three Planes	1200	0.000655	1832061.07	--	--	
Femur15	0.03000	0.01250	0.05600	0.00100	Circles	1.6 mm Spacing	ar Pattern (Une	Three Planes	300	0.000655	458015.267	1.08E-06	1.93E-05	25 GPa
	0.03000	0.01250	0.05600	0.00100	Circles	1.6 mm Spacing	ar Pattern (Une	Three Planes	600	0.000655	916030.534		0.00E+00	
	0.03000	0.01250	0.05600	0.00100	Circles	1.6 mm Spacing	ar Pattern (Une	Three Planes	900	0.000655	1374045.8		0.00E+00	
	0.03000	0.01250	0.05600	0.00100	Circles	1.6 mm Spacing	ar Pattern (Une	Three Planes	1200	0.000655	1832061.07	--	--	
Femur16	0.03000	0.01250	0.05600	0.00100	Circles	1.4 mm Spacing	Linear Pattern	Three Planes	300	0.000655	458015.267		0.00E+00	Won't Run
	0.03000	0.01250	0.05600	0.00100	Circles	1.4 mm Spacing	Linear Pattern	Three Planes	600	0.000655	916030.534		0.00E+00	
	0.03000	0.01250	0.05600	0.00100	Circles	1.4 mm Spacing	Linear Pattern	Three Planes	900	0.000655	1374045.8		0.00E+00	
	0.03000	0.01250	0.05600	0.00100	Circles	1.4 mm Spacing	Linear Pattern	Three Planes	1200	0.000655	1832061.07	--	--	
Femur17	0.03000	0.01500	0.05600	0.00100	Circles	1.6 mm Spacing	Linear Pattern	Three Planes	300	0.000655	458015.267	1.16E-06	2.07E-05	20.35 GPa
	0.03000	0.01500	0.05600	0.00100	Circles	1.6 mm Spacing	Linear Pattern	Three Planes	600	0.000655	916030.534	2.42E-06	4.32E-05	
	0.03000	0.01500	0.05600	0.00100	Circles	1.6 mm Spacing	Linear Pattern	Three Planes	900	0.000655	1374045.8		0.00E+00	
	0.03000	0.01500	0.05600	0.00100	Circles	1.6 mm Spacing	Linear Pattern	Three Planes	1200	0.000655	1832061.07	--	--	
Femur18	0.03000	0.01600	0.05600	0.00100	Circles	1.6 mm Spacing	Linear Pattern	Three Planes	300	0.000655	458015.267	1.25E-06	2.24E-05	17.58 GPa
	0.03000	0.01600	0.05600	0.00100	Circles	1.6 mm Spacing	Linear Pattern	Three Planes	600	0.000655	916030.534	2.65E-06	4.74E-05	
	0.03000	0.01600	0.05600	0.00100	Circles	1.6 mm Spacing	Linear Pattern	Three Planes	900	0.000655	1374045.8	4.12E-06	7.36E-05	
	0.03000	0.01600	0.05600	0.00100	Circles	1.6 mm Spacing	Linear Pattern	Three Planes	1200	0.000655	1832061.07	5.63E-06	1.00E-04	

Appendix IV: Measured Pore Diameters

Axial	Coronal	Sagitall
0.898	0.792	0.908
0.868	0.781	0.811
0.866	0.862	0.938
0.833	0.856	0.862
0.868	0.800	0.857
0.863	0.763	0.841
0.815	0.839	0.832
0.859	0.781	0.820
0.798	0.818	0.774
0.851	0.828	0.870
0.851	0.823	0.774
0.872	0.799	0.778
0.859	0.841	0.789
0.866	0.883	0.858
0.875	0.839	0.812

Appendix V: Analysis of Variance for Pore Diameters

Analysis of Variance (One-Way)

Summary

Groups	*Sample size*	*Sum*	*Mean*	*Variance*
Axial	15	12.842	0.85613	0.00061
Coronal	15	12.305	0.82033	0.00116
Sagitall	15	12.524	0.83493	0.00236

ANOVA

Source of Variation	*SS*	*df*	*MS*	*F*	*p-level*	*F crit*
Between Groups	0.00972	2	0.00486	3.53009	0.03828	4.30012
Within Groups	0.05783	42	0.00138			
Total	0.06755	44				

Appendix VII: Graphical Results of Compression Tests

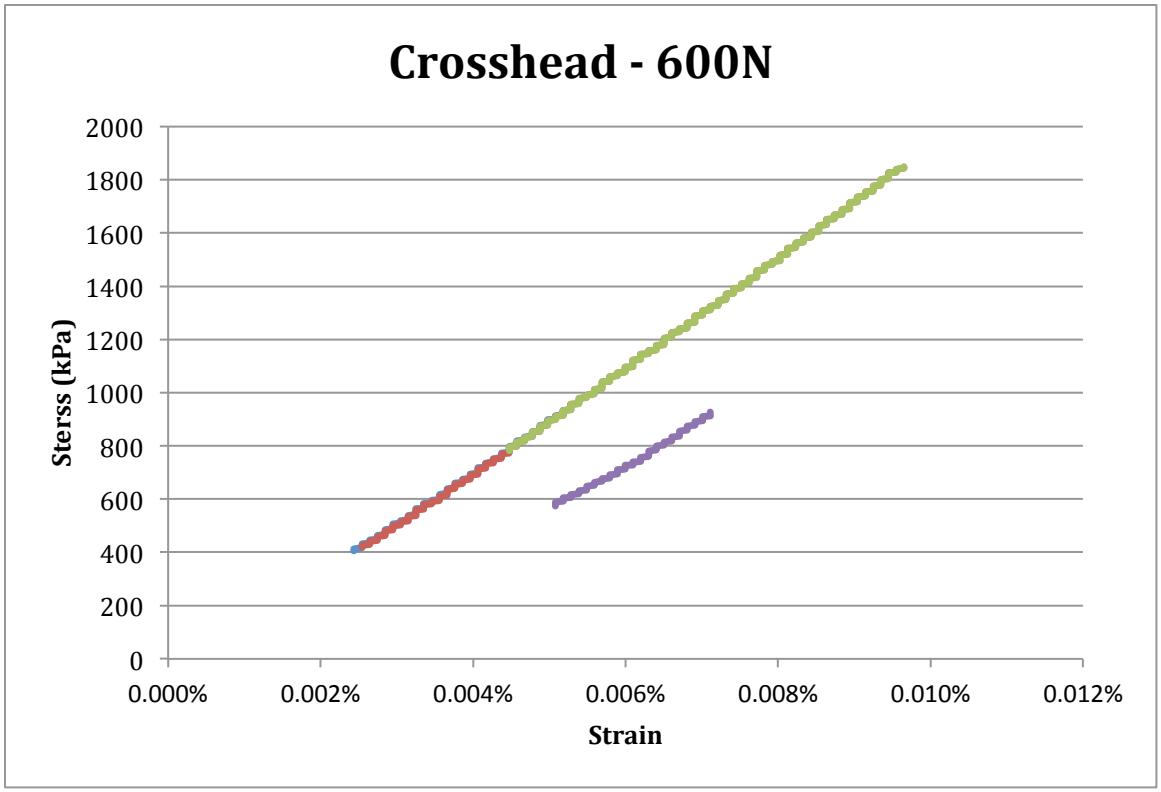

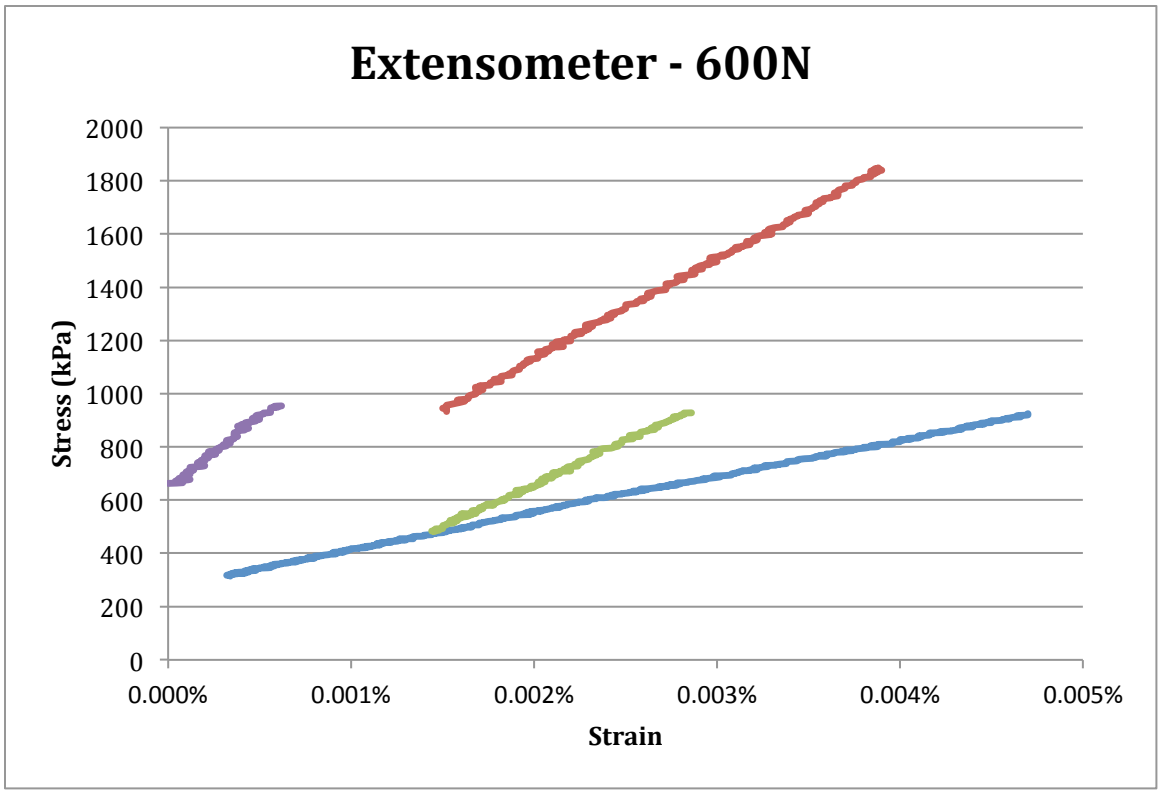

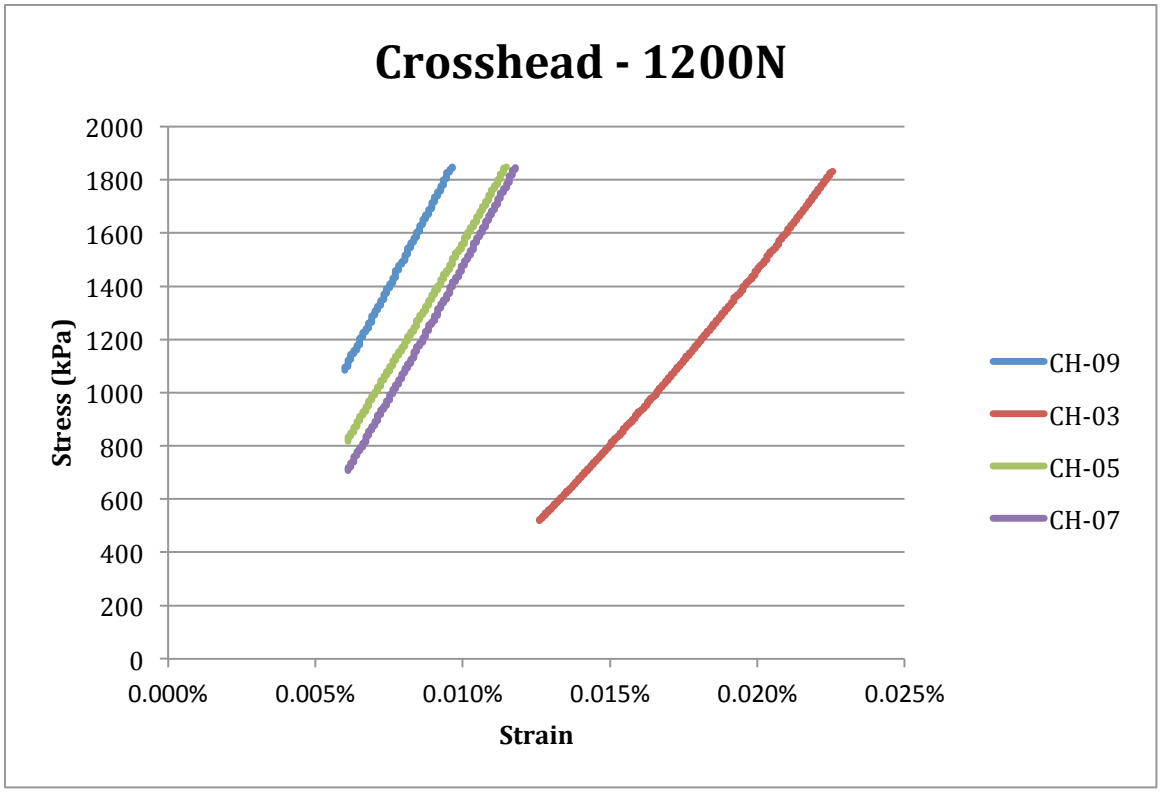
Crosshead - 1200N
2000
1800
1600
1400
1200
1000
800
600
400
200
0
Stress (kPa)
0.000%
0.005%
0.010%
0.015%
0.020%
0.025%
Strain
CH-09
CH-03
CH-05
CH-07

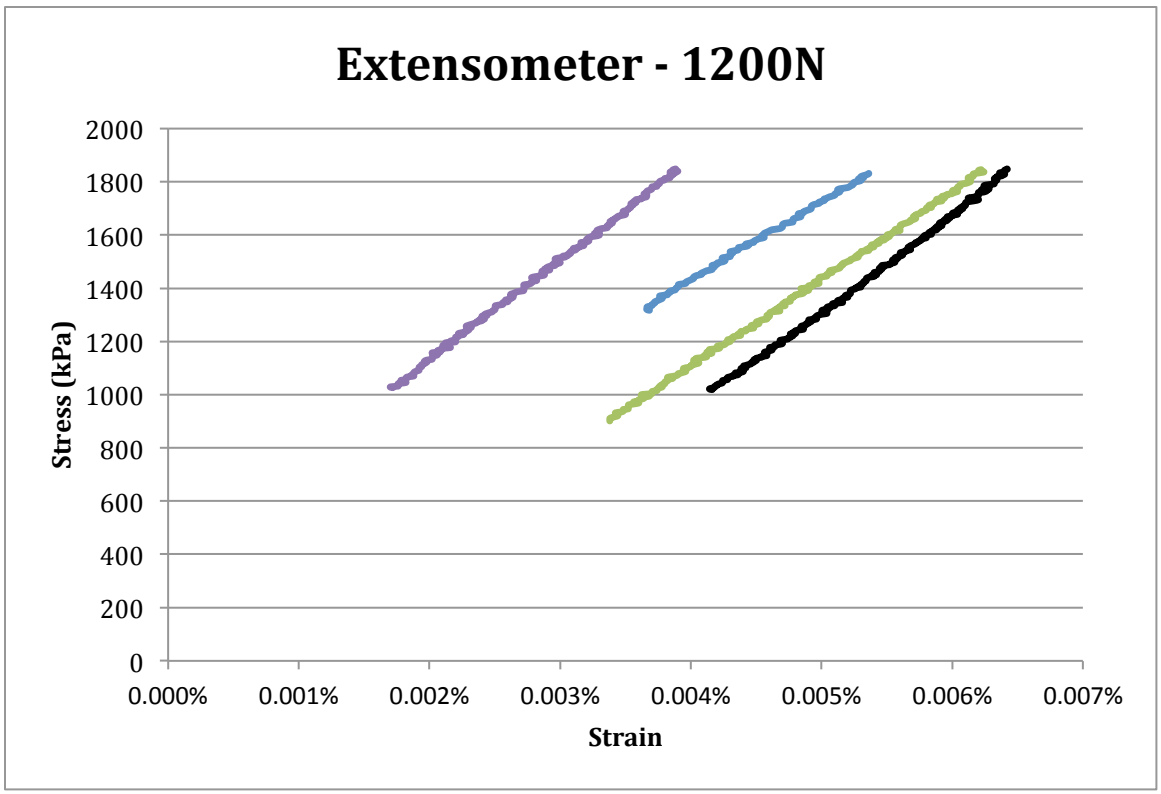
Extensometer - 1200N
2000
1800
1600
1400
1200
1000
800
600
400
200
0
Stress (kPa)
0.000%
0.001%
0.002%
0.003%
0.004%
0.005%
0.006%
0.007%
Strain

REFERENCES:

[1] Mavcic, Blaz, and Vane Antollic. "Optimal Mechanical Environment of the Healing Bone Fracture/Osteotomy." *International Orthopaedics* 36 (2012): 689-95.

[2] Martini F., & Nath J. L. (2009). Fundamentals of Anatomy and Physiology 8e. San Francisco, CA: Pearson Education Inc.

[3] Bosco, Ruggero, Jeroen Beucken, and Sander Leeuwenburgh. "Surface Engineering for Bone Implants: A Trend from Passive to Active Surfaces." *Coatings* 2 (2012): 95-119.

[4] Bosco, Ruggero, Jeroen Beucken, and Sander Leeuwenburgh. "Surface Engineering for Bone Implants: A Trend from Passive to Active Surfaces." *Coatings* 2 (2012): 95-119.

[5] Sargeant, Timothy, Mustafa Guler, and Scott Oppenheimer. "Hybrid Bone Implants: Self-Assembly of Peptide Amphiphile Nanofibers within Porous Titanium." *Biomaterials* 29 (2008): 161-71.

[6] "Metastatic Bone Disease-OrthoInfo - AAOS." *Metastatic Bone Disease-OrthoInfo - AAOS*. N.p., n.d. Web. 21 Nov. 2013.

[7] Sargeant, Timothy, Mustafa Guler, and Scott Oppenheimer. "Hybrid Bone Implants: Self-Assembly of Peptide Amphiphile Nanofibers within Porous Titanium." *Biomaterials* 29 (2008): 161-71.

[8] Pratt, Rebecca. "Bone as an Organ". AnatomyOne. Amirsys, Inc. Retrieved 2013-11-11.

[9] Bolanowski, Wojciech; Śmiszkiewicz-Skwarska, Alicja; Polguj, Michał; Jędrzejewski, Kazimierz S (2005). "The occurrence of the third trochanter and its correlation to certain anthropometric parameters of the human femur" (PDF). Folia Morphol. 64 (3): 168–175.

[10] Duda, G., E. Schnieder, and E. Chao. "Internal Forces and Moments in the Femur during Walking." *Journal of Biomechanics* 30.9 (1997): 933-41. Web.

[11] Bandyopadhyay, Amit, Felix Espana, Vamsi Balla, and Susmita Bose. "Influence of Porosity on Mechanical Properties and In Vivo Response of Ti6Al4V Implants." *Acta Biomater* 6.4 (2009): 1640-648. Web.

[12] Zysset, P., E. Guo, E. Hoffler, K. Moore, and S. Goldstein. "Elastic Modulus and Hardness of Cortical and Trabecular Bone Lamellae Measured by

Nanoindentation in the Human Femur." *Journal of Biomechanics* 32.10 (1999): 1005-012. Web.

[13] Besier, T., M. Fredericson, G. Gold, and G. Beaupre. "Knee Muscle Forces during Walking and Running in Patellofemoral Pain Patients and Pain-free Controls." *Journal of Biomechanics* 42.7 (2009): 898-905. Web.

[14] Fartash, A., M. Grimsditch, and E. Fullerton. "Breakdown of Poisson's Effect in Nb/Cu Superlattices." *The American Physical Society* 49.19 (1993): 123-29. Web.

[15] Zhao, Jun, Shu Ma, and Xue Wei. "Finite Element Analysis of Femur Stress under Bending Moment and Compression Load." *Biomedical Engineering and Informatics* (2009): 1-4. *IEEE*. Web.

[16] Zhao, Jun, Shu Ma, and Xue Wei. "Finite Element Analysis of Femur Stress under Bending Moment and Compression Load." *Biomedical Engineering and Informatics* (2009): 1-4. *IEEE*. Web.

[17] Parthasarathy, Jayanthi, Binil Starly, and Shivakumar Raman. "A Design for the Additive Manufacture of Functionally Graded Porous Structures with Tailored Mechanical Properties for Biomedical Applications." *Journal of Manufacturing Processes* 13 (2011): 160-70. Web.

[18] Montgomery, Douglas C., George C. Runger, and Norma Faris Hubele. *Engineering Statistics*. New York: John Wiley, 2001. Print.

[19] Bandyopadhyay, Amit, Felix Espana, Vamsi Balla, and Susmita Bose. "Influence of Porosity on Mechanical Properties and In Vivo Response of Ti6Al4V Implants." *Acta Biomater* 6.4 (2009): 1640-648. Web.

[20] Christensen, R. M. *Mechanics of Composite Materials*. New York: Wiley, 1979. Print.

[21] "Concentric Cylinder Assemblage (CCA) Model." *National Program on Technology Enhanced Learning*. Module 7: Micromechanics. Lecture 29, n.d. Web. 5 Mar. 2014.

[22] "DMLS or EBM? Which System Is Best?" *NetFabb*. Morris Technologies, n.d. Web. 14 Mar. 2014.